7-23-2003

Particle identification with aerogel Ĉerenkov detectors

Michael Carl
Florida International University

DOI: 10.25148/etd.FI14052575

FLORIDA INTERNATIONAL UNIVERSITY

Miami, Florida

PARTICLE IDENTIFICATION WITH AEROGEL ČERENKOV DETECTORS

A thesis submitted in partial fulfillment of the

requirements for the degree of

MASTER OF SCIENCE

in

PHYSICS

by

Michael Carl

2003

To: Dean R. Bruce Dunlap
College of Arts and Sciences

This thesis, written by Michael Carl, and entitled Particle Identification with Aerogel Čerenkov Detectors, having been approved in respect to style and intellectual content, is referred to you for judgment.

We have read this thesis and recommend that it be approved.

Brian Raue

Pete Markovitz

Abdelhamid Meziani

Joerg Reinhold, Major Professor

Date of Defense: July 23, 2003

The thesis of Michael Carl is approved.

Dean R. Bruce Dunlap
College of Arts and Sciences

Dean Douglas Wartzok
University Graduate School

Florida International University, 2003

ACKNOWLEDGMENTS

I would like to thank my adviser, Dr. Reinhold, for both his encouragement and inspiration in times of high productivity, as well as his patience in times of less productivity over the last four years.

Furthermore, I would like to thank the thesis committee for taking the time to help me prior to the date of the defense with corrections and suggestions toward my work.

Special thanks also to my co-workers and friends here at FIU, who made my time here more than just a work experience.

ABSTRACT OF THE THESIS

PARTICLE IDENTIFICATION WITH AEROGEL ČERENKOV DETECTORS

by

Michael Carl

Florida International University, 2003

Miami, Florida

Professor Joerg Reinhold, Major professor

Two detectors for charged particle identification have been built and tested. First, a test setup for a diffusion box threshold detector, using a 5 cm thick aerogel radiator has been designed and tested at the KEK PS facility in Japan. Using white Millipore paper as a diffuse reflector inside a diffusion box, the Čerenkov light gets scattered randomly until it hits one of the photomultipliers. On average up to 20 photoelectrons detected for pions at 1.2 GeV/c have been observed. Second, collection of Čerenkov light with an acrylic wavelength shifting plate was investigated. The test setup consisted of a plate, 30 cm long, 10 cm wide, and 1 cm thick placed behind a 5 cm deep stack of aerogel tiles. On the long ends the wavelength shifter was read out by two 5-inch photomultipliers. The response of the system to pions and protons at 1.2 GeV/c momentum was measured at the KEK PS facility in Japan. On average 6 photoelectrons radiated in the aerogel could be detected.

TABLE OF CONTENTS

LIST OF FIGURES

FIGURE PAGE

1 Introduction

1.1 Conceptual breakdown of the goal

Particle identification plays a crucial role in the data analysis in nuclear and particle physics. Such an experiment is the 'microscope' with which physical processes can be studied by detecting the components of a scattering reaction of a probe onto the target to be tested. The electron accelerator facility at the Thomas Jefferson National Accelerator Facility (Jlab), Virginia is an example of such a scattering probe. The electrons can be accelerated to momenta up to 6 GeV/c. This corresponds to a De Broglie wavelength of 2.1×10^{-16} meters, which is a measure of the resolution that can be achieved in such experiments. These electrons are incident on the target material within the sheltered experimental halls (HALL A, HALL B or HALL C). A particular nuclear reaction or a combination of different nuclear reactions creates a flux of hadrons with different momenta and directions filling the hall. The short lifetime of some of the exotic hadrons (e.g. the mean lifetime of a kaon is 1.24×10^{-8} seconds) restricts the maximum flight path available for time-of-flight (TOF) analysis. Furthermore, as the speed of different hadrons approaches asymptotically toward the speed of light, the flight time difference between different particles becomes restrictively small (e.g. for a flight path of only 2.2 m internal to the HMS detector stack used at Jlab) to incorporate a hardware trigger on TOF. Another option would be on-line computer analysis of these time-of-flight counters. However, due to the high rate of unwanted particle background (such as pions when looking for (e,e'K)), the computer dead-time for the time-of-flight analysis would severely limit the data acquisition. Therefore, a hardware particle veto (not involving TOF), that is capable of identifying background particles without using any computer calculations, is necessary.

1.2 Auxiliary particle identification

The identification of charged particles with a hardware trigger is most readily done in two parts:

- First, a magnet of given curvature and magnetic strength, B, bends the reaction particles of unknown momenta into a section of a circular path of radius R (see for example the magnet shown in Fig. 6). Therefore, one can determine (within a certain acceptance) the momentum of the particles that are able to travel through the magnet by:

$$\frac{p}{q} = BR \tag{1}$$

  where p is the momentum and q is the charge of the unknown particle.

- Second, with the momentum pre-selected by the magnet, additional knowledge of the particle's velocity (and charge, which is equal to e for our purposes) permits the determination of the mass and thus unambiguous identification of the particular particle type that passed through the detector.

This thesis summarizes the planning, development and testing of two different designs of detectors for such velocity determination, both based on the emission of Čerenkov radiation.

2 Physics principles behind Čerenkov detectors

2.1 Čerenkov radiation

The physical process underlying the Čerenkov detector is Čerenkov radiation. When a charged particle travels through a medium (such as aerogel) it electromagnetically interacts with the atomic electrons. If the speed of the particle within the medium of index of refraction n is greater than the local phase velocity of light (c/n), this interaction leads to a coherent light cone called Čerenkov radiation. However, if the speed of the particle is lower than the phase velocity of light within the medium, no such radiation is emitted. This dependence on the particle's velocity is exploited in the so-called "threshold detector", where the velocity of the particle can be determined to be above or below a certain threshold velocity. A graph showing the threshold velocity for different radiator media and different particle momenta is shown in Fig. 1.

A further property of Čerenkov radiation is the dependence of the opening angle of the light cone on the velocity of the particle [1]:

$$\theta_c = \arccos\left(\frac{1}{n\beta}\right) \tag{2}$$

where $\beta = v/c$

By projecting the light cone into a two dimensional ring and determining its radius, the opening angle can be determined and the velocity therefore calculated from Eq.(2). A graph showing the opening angle of the light cone for pions between 0.75 GeV/c (β=0.983) and 1.35 GeV/c (β=0.995) versus β for $n = 1.055$ and $n = 1.015$ is shown in Fig. 2. Notice that the most prominent dependence of the Čerenkov angle on the velocity is near the Čerenkov threshold.

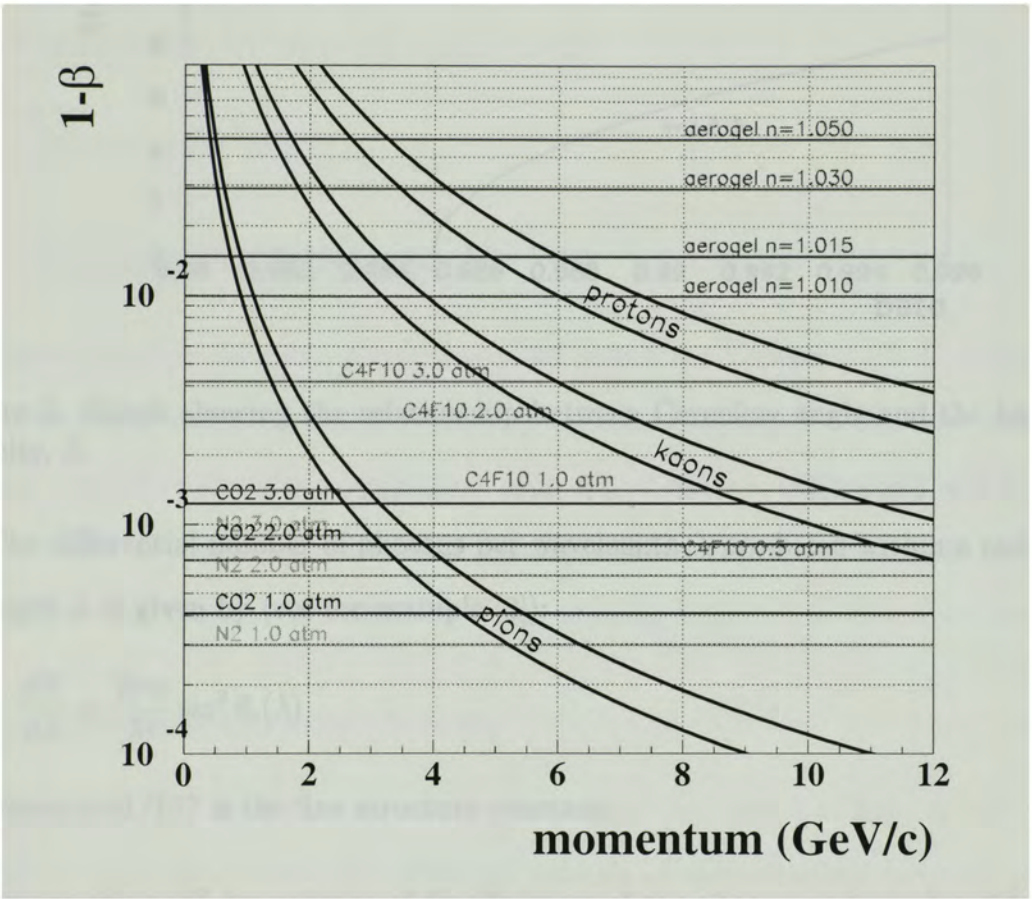

Figure 1: Graph showing the relationship between momentum and the hadron velocity for the SHMS. Also shown are the threshold velocities for some assorted radiators.

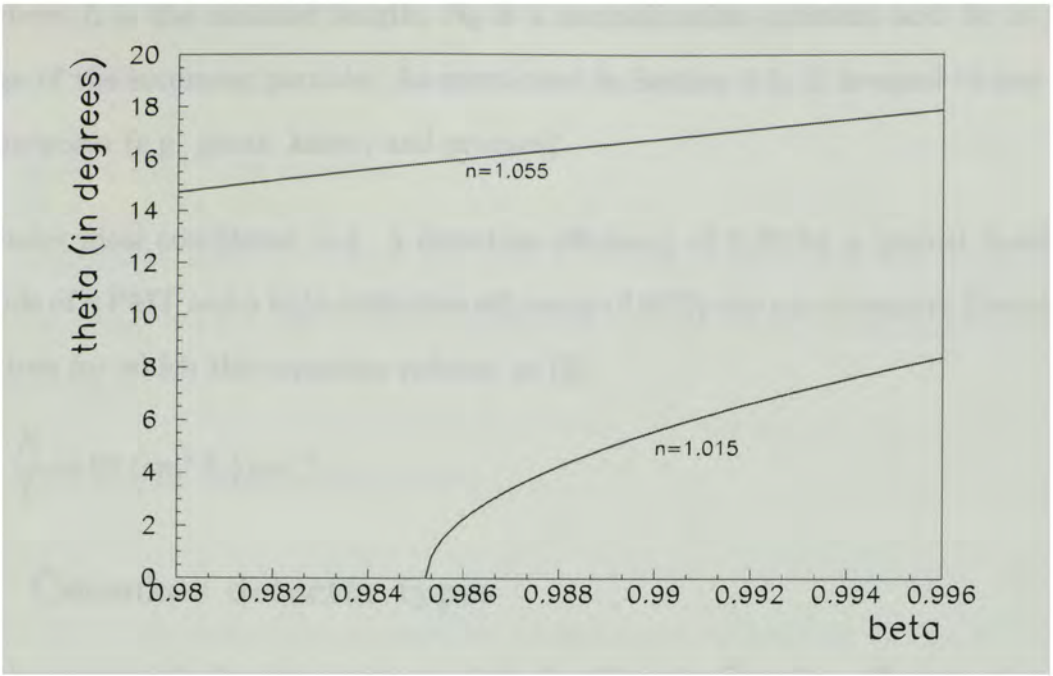

Figure 2: Graph showing the relationship between Čerenkov angle and the hadron velocity, β.

The differential number of photons per wavelength λ produced within a radiator of length L is given by (see for example [2]):

$$\frac{dN}{d\lambda} = \frac{2\pi\alpha}{\lambda^2} \sin^2 \theta_c(\lambda) \tag{3}$$

where α=1/137 is the fine structure constant.

Due to the $1/\lambda^2$ dependence of Eq.(3), most of the photons are produced in the UV range. Therefore, it is an important requirement of every Čerenkov detector to have a high detection efficiency in this wavelength band.

Integrating this equation over λ, as well as the detection and collection efficiencies, the total number of detected photoelectrons is given by [2]:

$$N = N_0 L Z^2 \left\langle \sin^2 \theta_c \right\rangle \tag{4}$$

where L is the radiator length, N_0 is a normalization constant and Ze is the charge of the incoming particle. As mentioned in Section 1.1, Z is equal to one for our purposes (e.g. pions, kaons, and protons).

Under ideal conditions (e.g. a detection efficiency of 0.27 for a typical bi-alkali cathode of a PMT and a light collection efficiency of 90%) one can construct Čerenkov detectors for which this equation reduces to [2]:

$$\frac{N}{L} = 90 \left\langle \sin^2 \theta_c \right\rangle \mathrm{cm}^{-1} \tag{5}$$

2.2 Čerenkov detector types

The three principle detector concepts that all utilize the Čerenkov effect are threshold, differential and Ring-Imaging (RICH) Čerenkov detectors. The first and the last are related to the new designs that were tested for this thesis, and will be discussed below in detail. A differential Čerenkov detector is designed such that the light collection efficiency is a function of the opening angle of the Čerenkov cone.

2.2.1 Threshold Čerenkov detector

The threshold Čerenkov detector takes advantage of the fact that light is only radiated if the particle is above the threshold velocity of the radiating material, which has a given index of refraction, n. For example, for a 1.2 GeV/c mixed hadron beam of protons, kaons and pions (such as encountered in the hypernuclear experiment described in Section 3.1) an aerogel radiator of index of refraction of 1.055 serves as a discriminator of pions that are above threshold as opposed to kaons and protons that are below threshold at this momentum (see Fig. 1). The greatest challenge for every Čerenkov detector is the collection of the Čerenkov radiation, which is then

incident onto a photomultiplier tube (see below) for detection. Some of the strategies for an efficient light collection relevant for this discussion are the use of:

- Mirrors that focus the light.
- Wavelength shifters in which the light is converted into a different wavelength band and transported (see for example the second detector described later in the text).
- Diffusion boxes (explained below).

Only the last of theses example for light collection, the diffusion box, will be important for our design of a partitioned threshold aerogel detector. Such a diffusion box consists of three major pieces:

- The radiator. Different radiator types exist in all phases: gas, liquid and solid. An example of a solid radiator is aerogel. In general, the index of refraction of hydrophobic aerogel (produced by [3]) ranges from 1.015 to 1.055 (extreme values for n for aerogel range from 1.01 to 1.06). Therefore, aerogel can be used to separate pions from kaons between 0.5 GeV/c up to 2.5 GeV/c and kaons from protons between 1.5 GeV/c up to 5.5 GeV/c. To achieve an even lower index of refraction, a gas such as C_4F_{10} with index of refraction of 1.0014 at 1 atm can be used. With such a radiator one can separate pions from kaons between 2.25 GeV/c up to 9.0 GeV/c and kaons from protons between 9.0 GeV/c up to 17.5 GeV/c. Other radiators are available and shown in Fig. 1 along with the corresponding operational ranges.
- The diffusion box. In the diffusion box, the light gets scattered randomly until it hits one of the photomultipliers (see below). A critical measure of such a diffusion box is the ratio of active to passive area. The active area is defined

as the area covered by the photomultipliers, whereas all other surfaces within the box are defined as the passive area. The higher this ratio is, the higher the probability for detection of a given photon. Furthermore, the reflectivity of the passive area is crucial for the collection efficiency of the detector.

- The photomultiplier tube (PMT). It is the PMT that ultimately detects the light by converting it into so called photoelectrons. A schematic figure of a PMT is shown in Fig. 3. When the photon hits the cathode of the PMT, an electron is knocked out via the photoelectric effect. This electron then gets accelerated by the potential difference between the cathode and the next stage and knocks out several more electrons. This process repeats through several stages, (10 stages for the Photonis XP4572B/D1 [4]) until an easily measurable signal of about 10^{-12} C is created. Typical photomultiplier bi-alkali cathodes have peak quantum efficiencies of 20 to 25% at 400 to 420 nm wavelength.

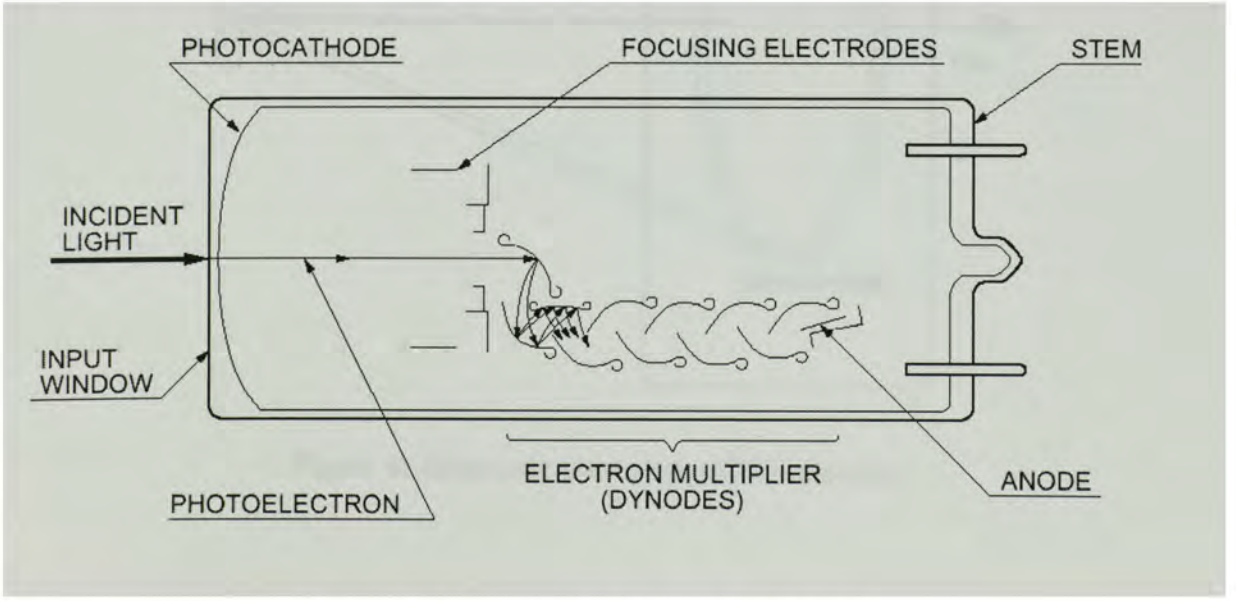

Figure 3: Schematics of a typical PMT [4].

For reference, examples of successful diffusion box threshold detectors at Jlab are given in [5],[6],[7].

2.2.2 RICH detector

Velocity discrimination with the RICH detector concept is done by measuring the opening angle of the Čerenkov cone. This is done by projecting the light cone either directly or with the help of mirrors into a two dimensional ring (see Fig. 4). The plane of projection is filled with highly segmented photon detectors. With the distance from the radiator to the plane known, the radius of the projected ring gives a measure for the opening angle θ_c. Using Eq.(2) one can therefore calculate β. The major components of the RICH detector are:

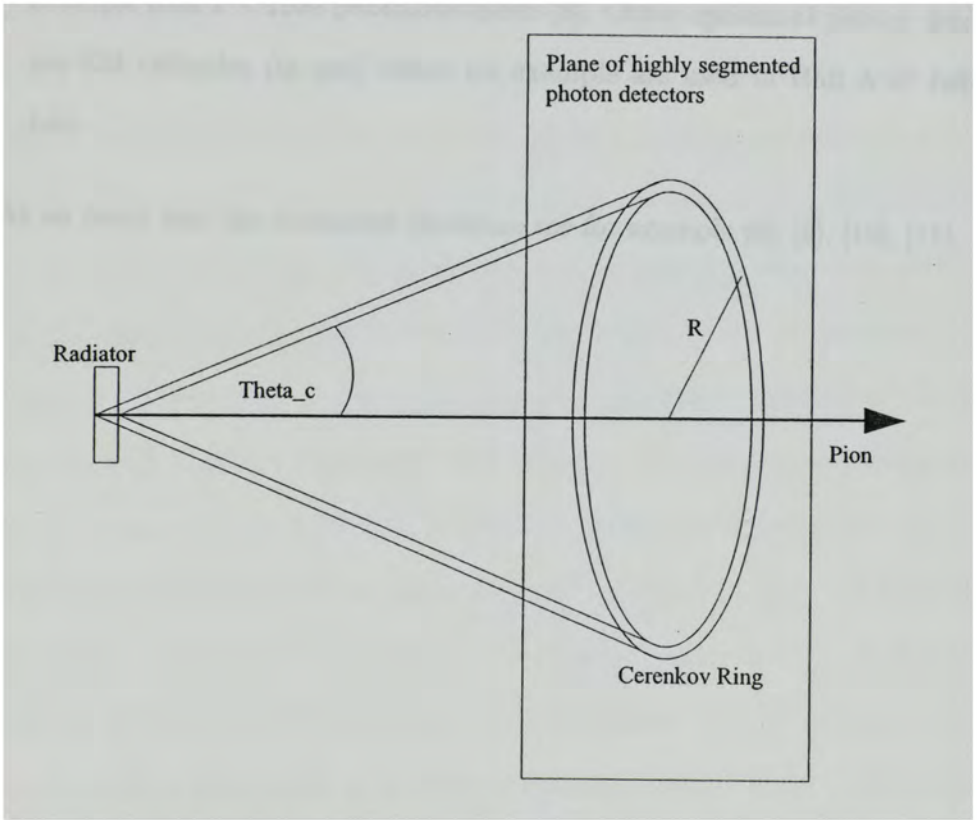

Figure 4: Schematic view of the RICH readout.

- The radiator. Depending on the type of experiment, and therefore momentum of the particles to be detected, all three different kinds, solid, liquid and gaseous mediums can be used as radiators.

- Light collectors or light focus. Usually mirrors are used.

- The plane of highly segmented photon detectors. This part of the RICH detector is what makes it more expensive and therefore less common than other detector types. In order to get a good spacial resolution, the Hermes RICH for example uses 2×1934 photomultipliers [8]. Other options of photon detectors are CsI cathodes (in gas) which for example are used in Hall A of Jefferson Lab.

As an entry into the numerous literature see for example [8], [9], [10], [11].

3 Physics motivation

3.1 Hypernuclear experiment

The main reaction in the hypernuclear experiment is kaon-electroproduction, (e,e'K^+), as shown in Fig. 5. The electron transfers part of its energy via a virtual photon to the proton, producing a strange-anti-strange quark pair. The anti-strange quark combines with one of the up quarks of the proton to form a kaon whereas the remaining up and down quark combine with the strange quark to form a lambda or sigma hyperon. For the upcoming E01-011 experiment at Jlab [12], two new spectrometers (see Fig. 6) have been developed, in order to achieve a momentum resolution of down to 300 keV/c. This would imply an improvement in resolution by a factor of 3 with respect to earlier experiments [13] where the best resolution was only 900 keV/c. With a momentum resolution of 300 keV/c, one will be able to measure binding energies with high precision and also observe the spin orbit splitting of the hypernuclei in a neutron rich environment. The negative arm of the spectrometer, the ENGE spectrometer, is tilted by 2.25 degrees in order to minimize the acceptance for electron bremsstrahlung, while preserving resolution. The positive kaon arm of the spectrometer, the HKS (High Resolution Kaon Spectrometer), is designed in such a way as to increase the coincidence rate between the ENGE and the HKS spectrometer while maintaining a momentum resolution of 2×10^{-4}. The expected rates for the two spectrometer arms are summarized in Table 1. In order to optimize the figure of merit, the optimal momentum range chosen for the experiment is around 1.2 GeV/c [12]. Given a data acquisition rate of 1-2 kHz, the requirement of an aerogel Čerenkov detector would be pion suppression of 10^{-4} at this momentum, in order to reduce the pion rate to a comparable level as the kaon rate.

Table 1: Expected singles rates for E01-011

Target	Beam Intensity (μA)	HKS e^+ rate (kHz)	HKS π^+ rate (kHz)	HKS K^+ rate (kHz)	HKS p rate (kHz)	Enge e^- rate (kHz)	Enge π^- rate (kHz)
^{12}C	30	-	420	0.38	150	1,000	2.8
^{28}Si	30	-	420	0.32	130	1,900	2.8
^{51}V	30	-	410	0.29	120	2,650	3.0

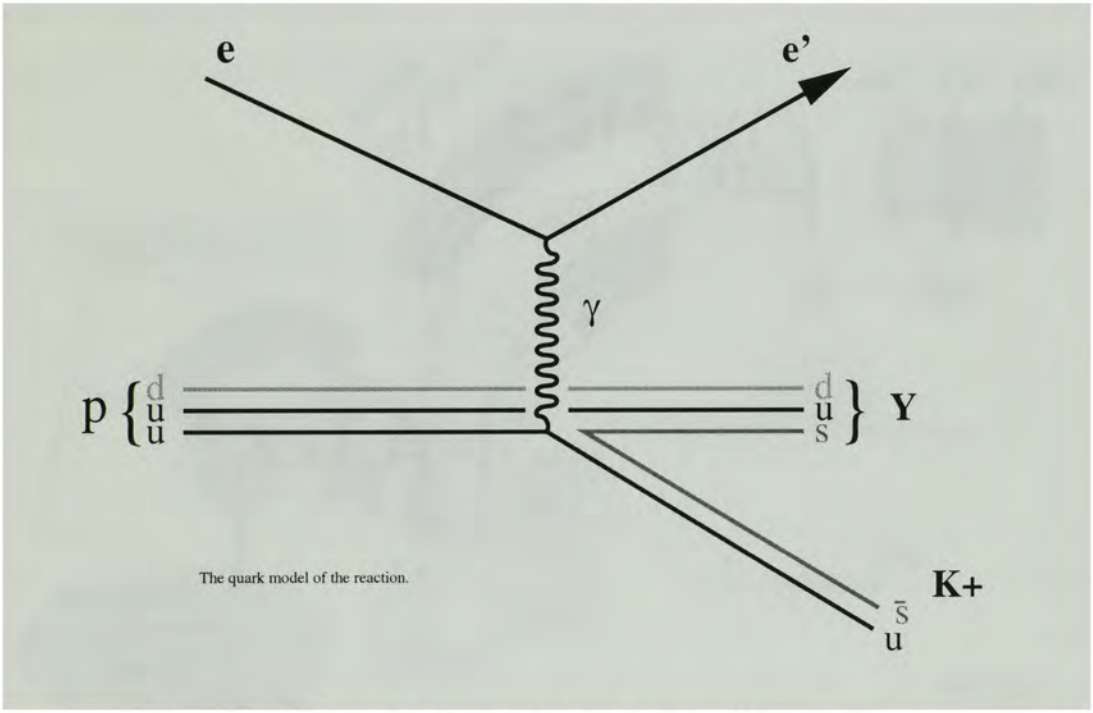

Figure 5: Schematic description of the (e,e'K^+) reaction.

3.2 Jefferson Lab upgrade

The Jefferson Lab upgrade from 6 GeV to 12 GeV, which is currently under discussion, would provide HALL C with a 10.9 GeV electron beam [14]. In a momentum range of 5.5 GeV to 9 GeV, however, kaon-proton separation is unfeasible with ordinary threshold detectors. From Fig. 1, one can see that in this momentum range there exists no radiator (save for pressurized gases, as shown Fig. 1, which are difficult and dangerous to operate) with an appropriate index of refraction such that kaons are above, and protons are below threshold. Furthermore, the restricted flight

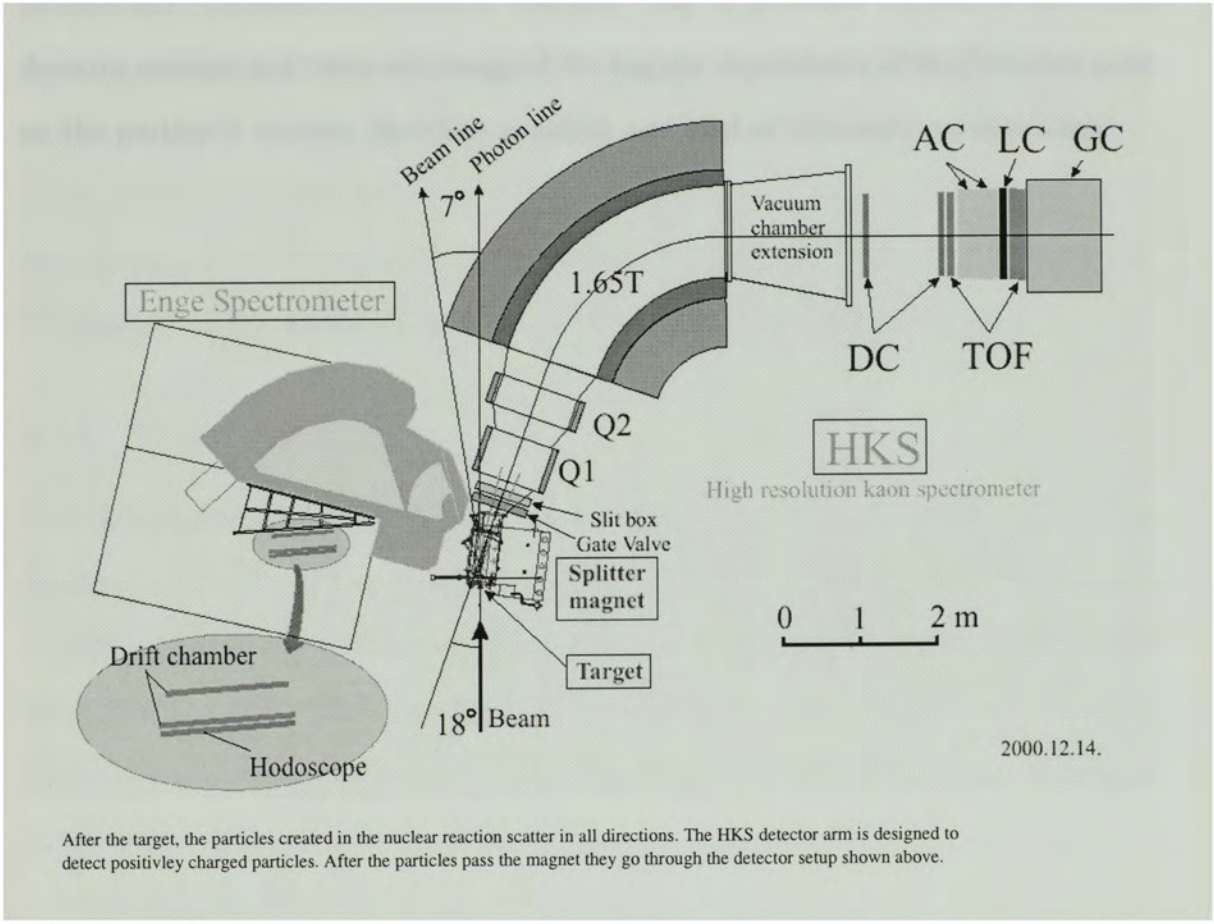

Figure 6: View of the hypernuclear spectroscopy system with the ENGE and HKS as electron and kaon spectrometers, respectively. Also shown are several detectors for particle identification: TOF (time-of-flight counter), AC (Aerogel Čerenkov counter).

path of the HMS or SHMS detector assembly makes time-of-flight analysis unfeasible, because the hadron velocity asymptotically approaches β=1 at this momentum. The second detector described below is designed in such a way as to fit the gap in the radiator selection and could be used as part of the proposed SHMS (Super High Momentum Spectrometer) detector assembly [14]. It is closely related to the RICH detector concept and takes advantage of the angular dependence of the Čerenkov cone on the particle's velocity, therefore avoiding any kind of threshold considerations.

4 Proposed detector designs

4.1 Partitioned threshold aerogel Čerenkov detector

As mentioned in Section 3.1, a pion suppression of 10^{-4} at 1.2 GeV/c with only a few percent kaon loss is required for the hyper-nuclear experiment. Under the predicted pion rate of 420 kHz, traditional threshold detectors such as described in Section 2.2 will not be able to provide such performances, because the high rate of pions will cause the electronic dead-time to conflict with the kaon data acquisition. In order to accommodate these requirements, a modified design of a diffusion box threshold Čerenkov detector containing 7 separated compartments was developed.

4.1.1 Detector description

The detector setup, which contains three identical layers, is shown in Fig. 7. The dimensions of each such layer are 1620 mm × 460 mm × 200 mm. The outer frame is built out of aluminum honey-comb panels in order to achieve a sturdy but light-weight design. Each side of the detector has 7 PMTs (which are separately equipped with magnetic shields) connected to the wall. In contrast to traditional open diffusion boxes, which are already in use at HALL C at Jlab [13], this system is partitioned into 7 compartments. The details of each individual compartment are discussed in Section 4.1.3. The partitioning will reduce the rate for each compartment by a factor of seven (assuming homogeneous flux over the detector area). A negative consequence of this partitioning is the increase in passive area, which reduces the collection efficiency by a factor of around 1.2 (described by the Monte-Carlo simulation described below) in comparison to the open design. A detailed simulation was used to predict the expected efficiency of the detector (see Section 4.1.2).

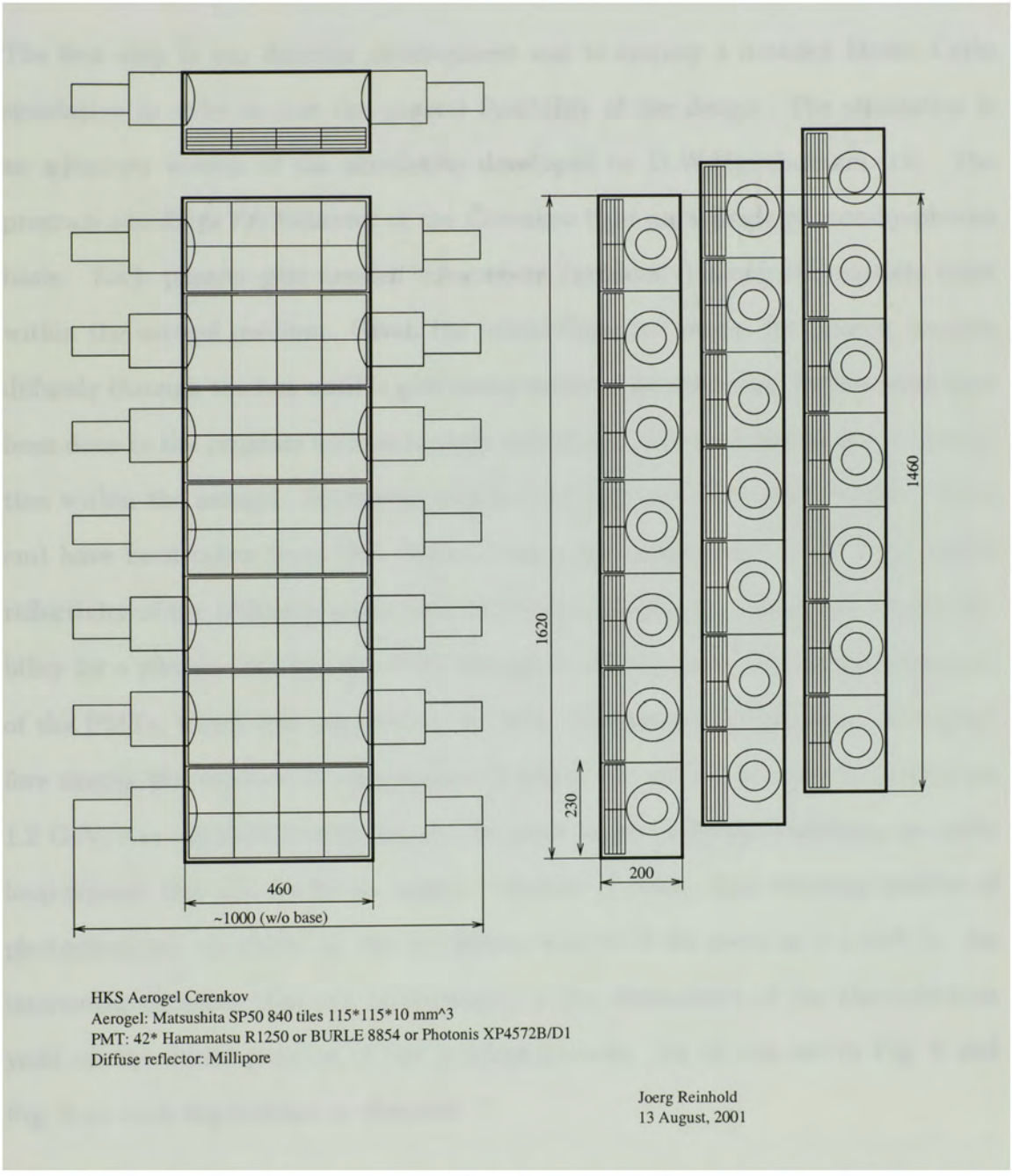

Figure 7: Schematic view of complete detector setup (compare Fig. 10). All dimensions are in mm. Left: Seven segments of one detector layer. Right: Relative positioning of the three layers. Particle flux is incident from the left.

4.1.2 Simulations

The first step in our detector development was to employ a detailed Monte Carlo simulation in order to test the general feasibility of the design. The simulation is an advanced version of the simulation developed by D.W.Higinbotham [15]. The program simulates the behavior of the Čerenkov light on a single photon-by-photon basis. Each photon gets created somewhere (randomly) along the particle track within the aerogel medium. Given the initial Čerenkov angle, the photon bounces diffusely through the box until it gets either detected or absorbed. Refinements have been done to the program such as directly taking into account scattering and absorption within the aerogel. Scattering length (2.5 cm) and absorption length (200.0 cm) have been taken from [16]. Other sources for absorption are the finite (98%) reflectivity of the Millipore paper and, of course, the quantum efficiency (the probability for a photon that hits the PMT window to be converted into a photoelectron) of the PMTs, which was assumed to be 24%. The number of photons (and therefore simply the number of computational loops) for one single pion of momentum 1.2 GeV/c is calculated using Eq.(3). In order to get sufficient statistics, an outer loop repeats this procees for an arbitary number of pions. The resulting number of photoelectrons calculated by the simulation was 19.76 for pions at 1.2 GeV/c. An interesting property that can be simulated is the dependence of the photoelectron yield on the initial position of the incident particle. As on can see in Fig. 8 and Fig. 9 no such dependence is observed.

4.1.3 Experimental setup and procedure

After sufficient evidence was found to motivate further investigations, stage two comprised the designing and building of a test setup in order to see its applicability in practice. A diffusion box test setup containing only one such partitioned com-

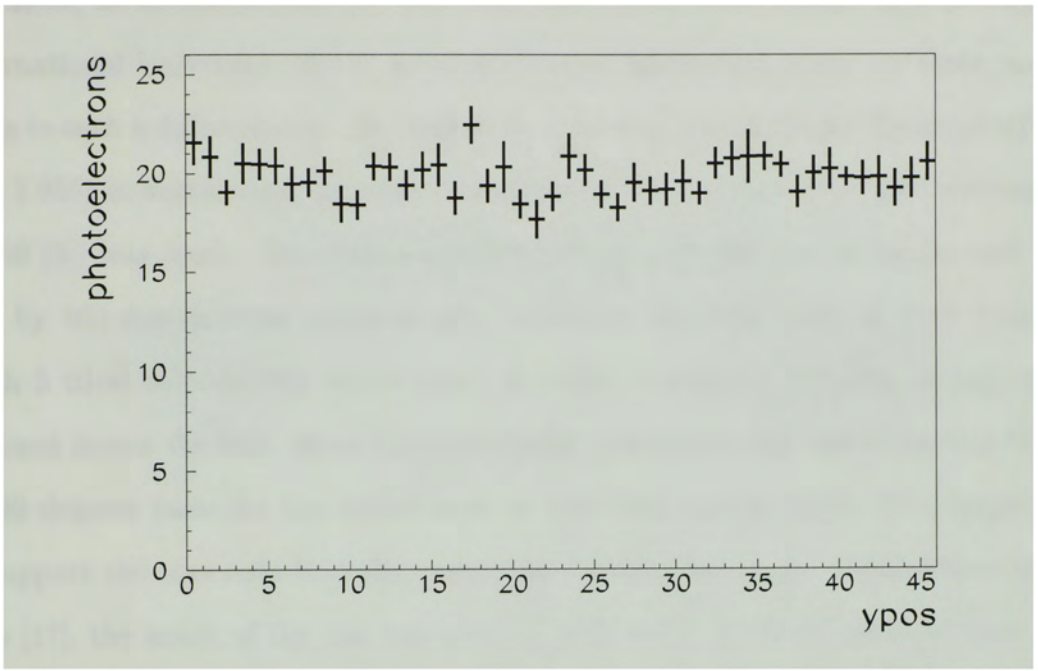

Figure 8: Simulated average number of photoelectrons versus y-position (in cm) of the incident particle.

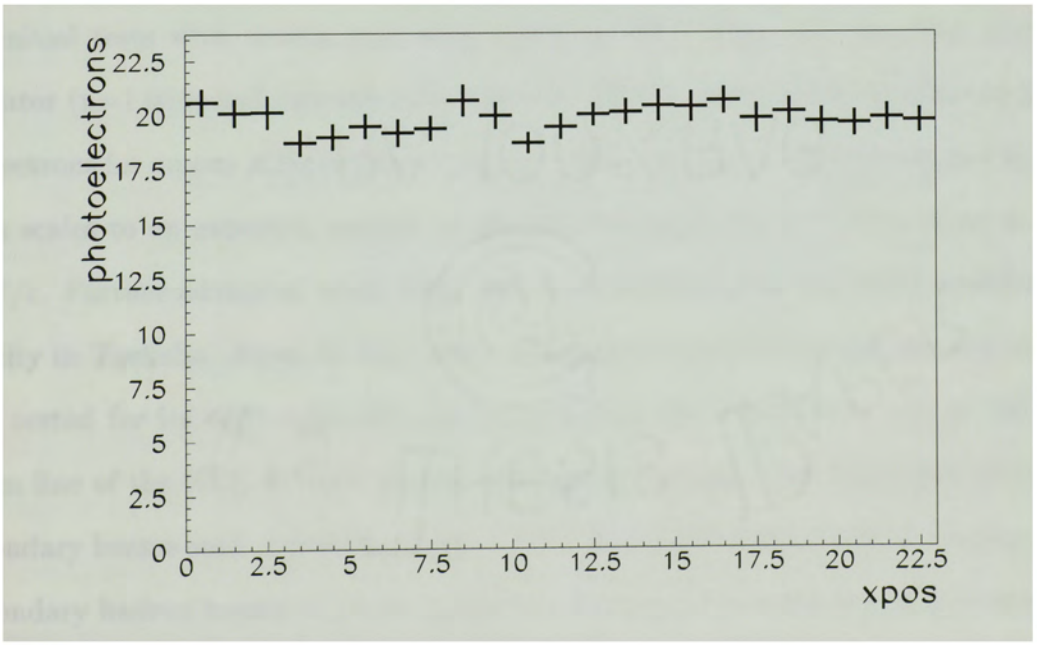

Figure 9: Simulated average number of photoelectrons versus x-position (in cm) of the incident particle.

partment, as shown in Fig. 10, was built and tested with cosmic rays at Florida International University (FIU). As mentioned in Section 2.2, there are three mayor parts to such a diffusion box. As a radiator, a stack of 5 aerogel tiles (index of refraction 1.055) in depth, each tile with dimensions of $115 \times 115 \times 10$ mm^3 (Matsushita SP-50 [3]) was used. The dimensions of the box were 200 mm in height and 230 mm by 460 mm in cross sectional area, therefore requiring a set of 2 by 4 stacks (each 5 tiles) to cover the entire area. In order to support the tiles, strings were spanned across the box. Since the operational position of this test setup was tilted by 90 degrees (save for the initial tests at FIU with cosmic rays), the strings had to support the tiles only laterally, except for the loading phase. Using double sided tape [17], the inside of the box was covered with white Millipore paper of pore size 0.22μm [18]. The stated reflectivity of the Millipore paper was 98% [19]. The two PMTs on each side of the detector were 130 mm Photonis tubes (XP4572B/D1 [4]) with a quantum efficiency of 24% at 420 nm and a typical gain of up to 10^7.

Initial tests with cosmic rays were taken at FIU. Using a 5 cm deep aerogel radiator (n=1.055) and running both tubes at -1900V, the number of detected photoelectrons for muons with average energy of 4 GeV was about 25 as shown in Fig. 11. This scales to an expected number of photoelectrons of about 23.4 for pions at 1.2 GeV/c. Further advanced beam tests have been conducted at the KEK accelerator facility in Tsukuba, Japan in May 2002. Along with other detectors, the test setup was tested for its light collection efficiency during the T500 beam test at the T1 beam line of the KEK 12 GeV proton synchrotron facility. This beam line provides secondary beams with momenta up to 2 GeV/c and a momentum bite of roughly 1%. Secondary hadron beams of pions, kaons and protons were extracted at momenta of 0.50, 1.05, 1.20, and 1.35 GeV/c. The detector test setup described above and several other prototype detectors were arranged downstream of a dipole magnet used

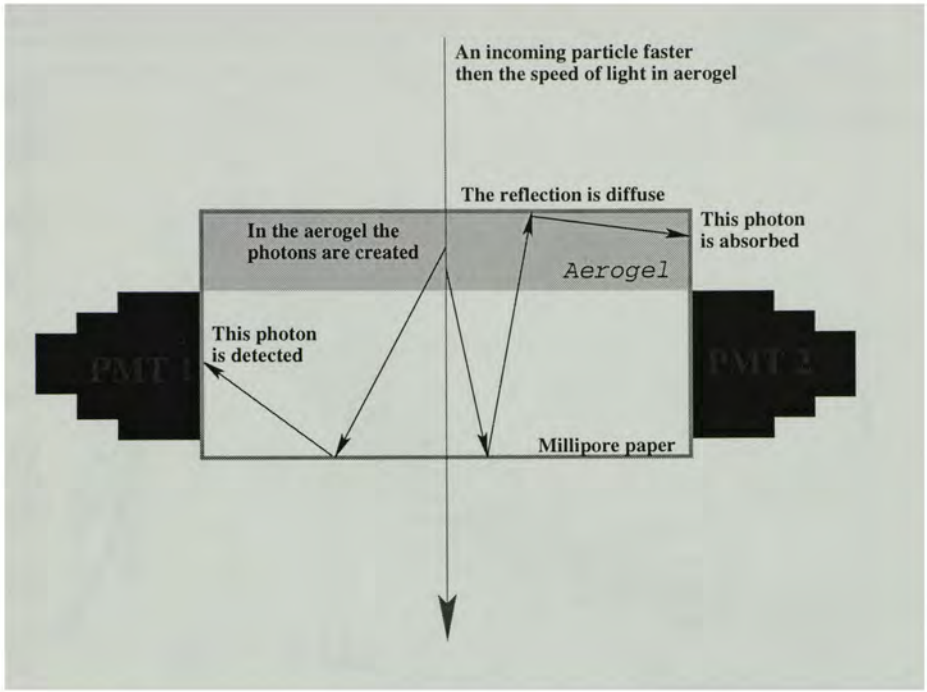

Figure 10: Schematic view of the test detector.

for momentum selection. Two small scintillator crosses in the front and the back of the detectors served as time-of-flight detectors for particle identification. These time of flight (TOF) detectors actively collimated the beam to an envelope of 4×4 cm^2. Fig. 12 shows the experimental setup. At all momenta, pions were above the aerogel's Čerenkov threshold, whereas kaons and protons were below threshold.

4.1.4 Analysis and results

A typical unbiased time-of-flight (TOF) distribution at 1.2 GeV/c is shown in Fig. 13. Due to the narrow momentum selection of 1% around 1.2 GeV/c by the TOF, pions (left peak) and protons (right peak) were unambiguously identified. A small number of kaons can be seen as a shoulder on the pion distribution. In order to clean this distribution from the typical pulse-height dependence of the TOF on the signal-pulse-height, (ADC), (see Fig. 14), corrections were done, assuming a Gaussian behavior

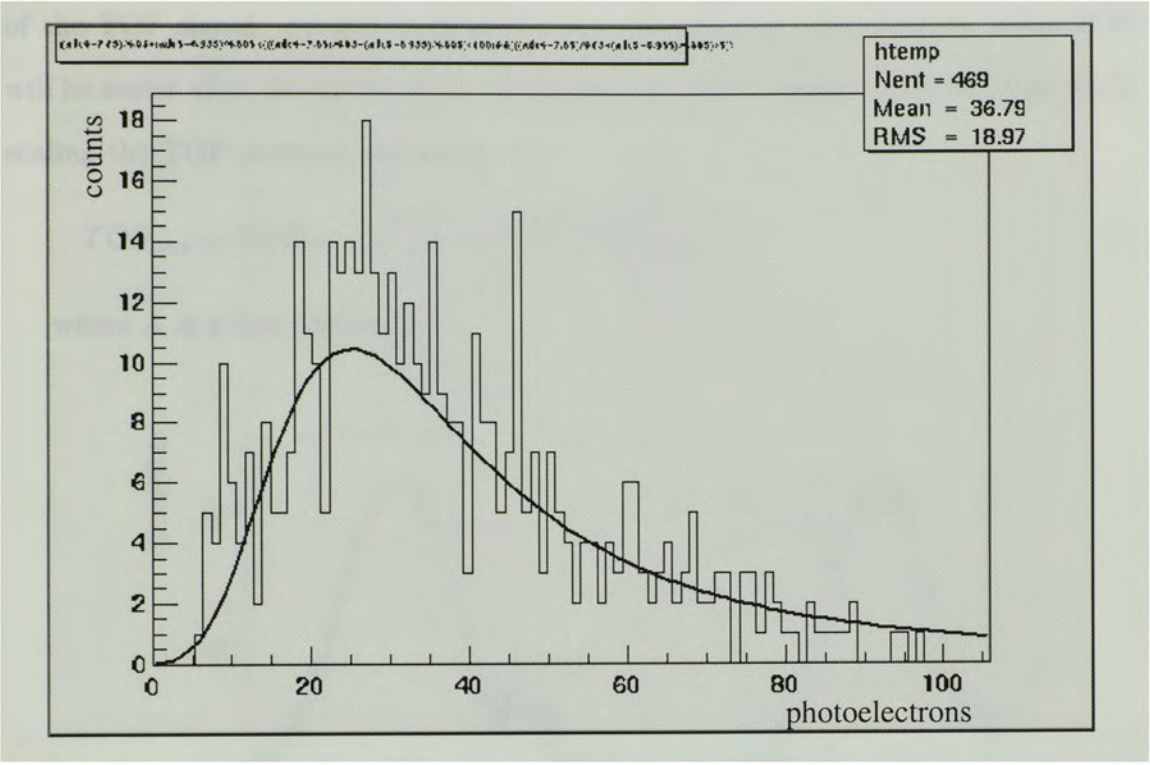

Figure 11: Distribution of the number of photoelectrons for the cosmic test.

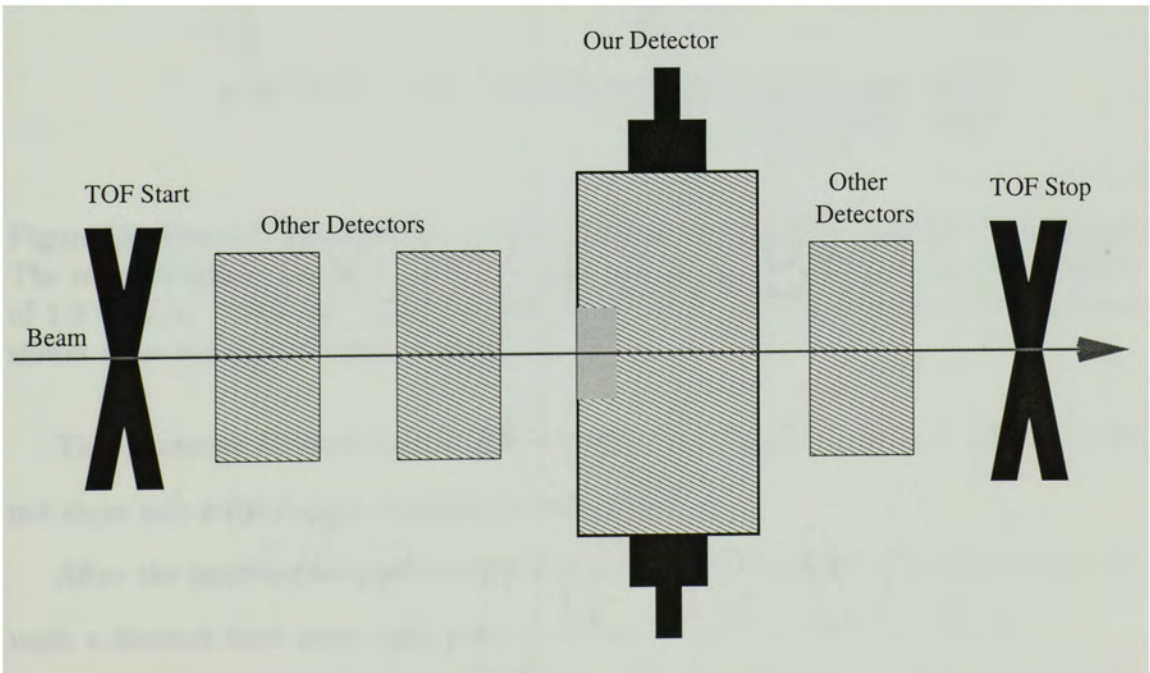

Figure 12: Schematic view of the experimental setup (not drawn to scale).

of the TOF signal. As will be shown below, the particle identification using TOF will be easier after the distributions are corrected. The n-tuples were rewritten while scaling the TOF counters according to:

$$TOF_{new} = TOF_{old} + \sqrt{A \times \ln(ADC/ADC_{min})} \tag{6}$$

where A is a free parameter.

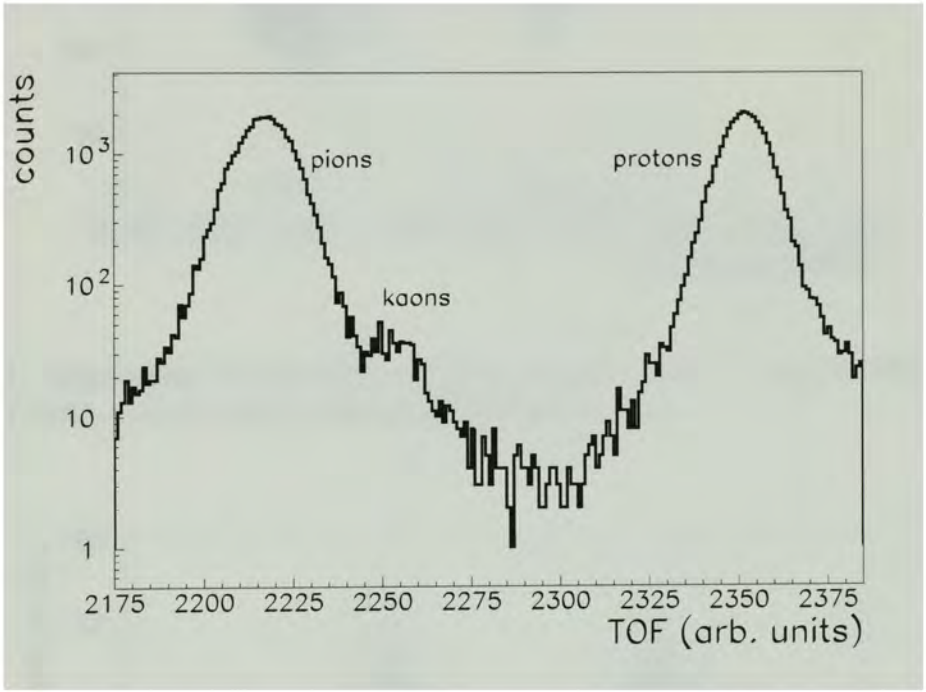

Figure 13: Time-of-flight distribution (TDC channel) before pulse-height corrections. The magnet selects particles with a narrow spread of (1%) around the central value of 1.2 GeV/c. With the same momentum, heavier particles such as protons move slower than the lighter pions or kaons.

The corrected distributions of ADC versus TDC, which are shown in Fig. 15, do not show any pulse-height dependence anymore.

After the appropriate pulse-height corrections are employed this distribution reveals a distinct kaon peak right next to the pion peak, as shown in Fig. 16.

For the later analysis, particle identification (PID) cuts were placed on these TOF distributions, along with cuts on similar threshold aerogel Čerenkov detectors in the

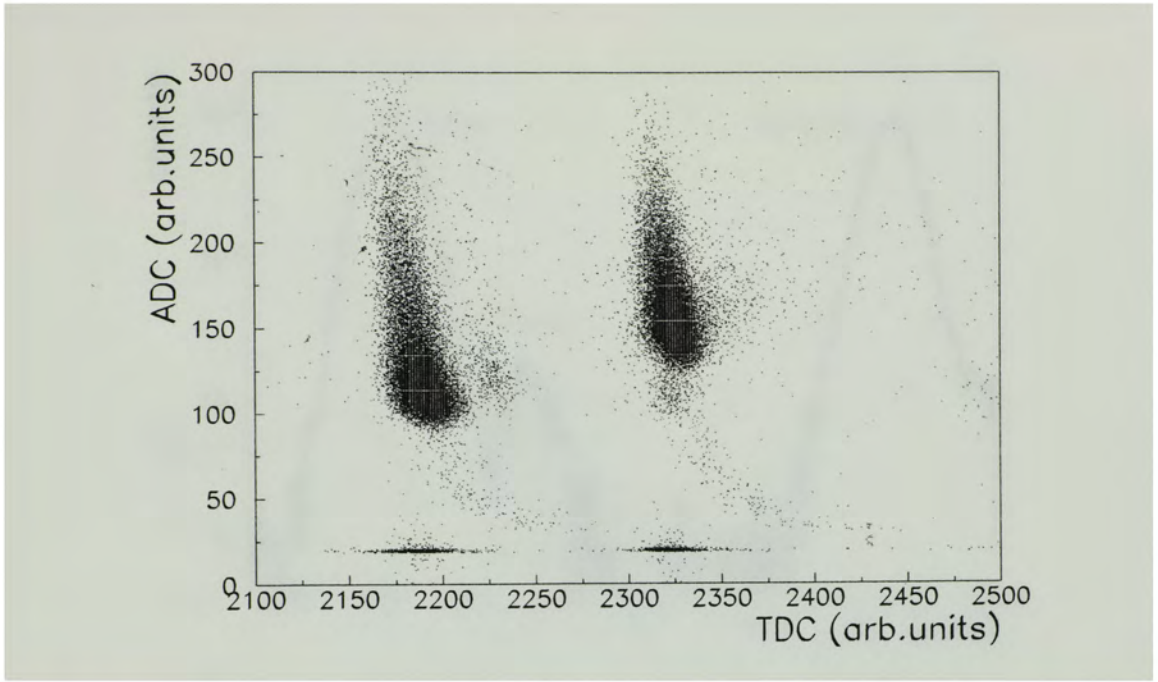

Figure 14: Dependence of the time-of-flight counters (TDC, x-axis) on the signal strength (ADC, y-axis) before pulse-height corrections.

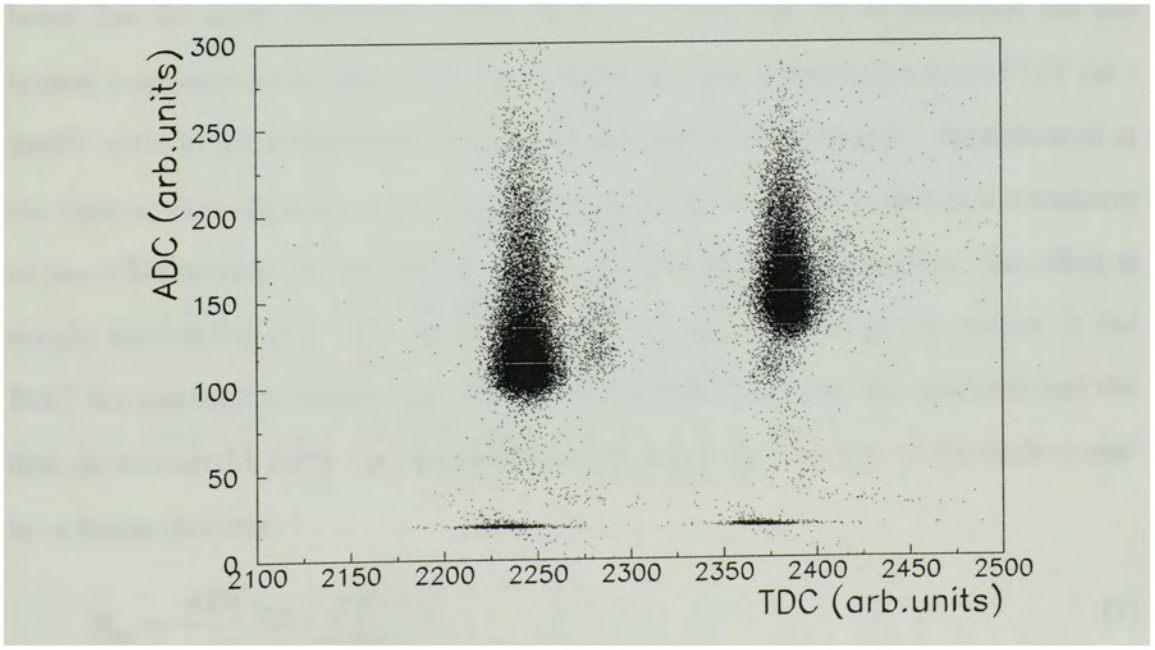

Figure 15: Dependence of the time-of-flight counters (TDC, x-axis) on the signal strength (ADC, y-axis) after pulse-height corrections.

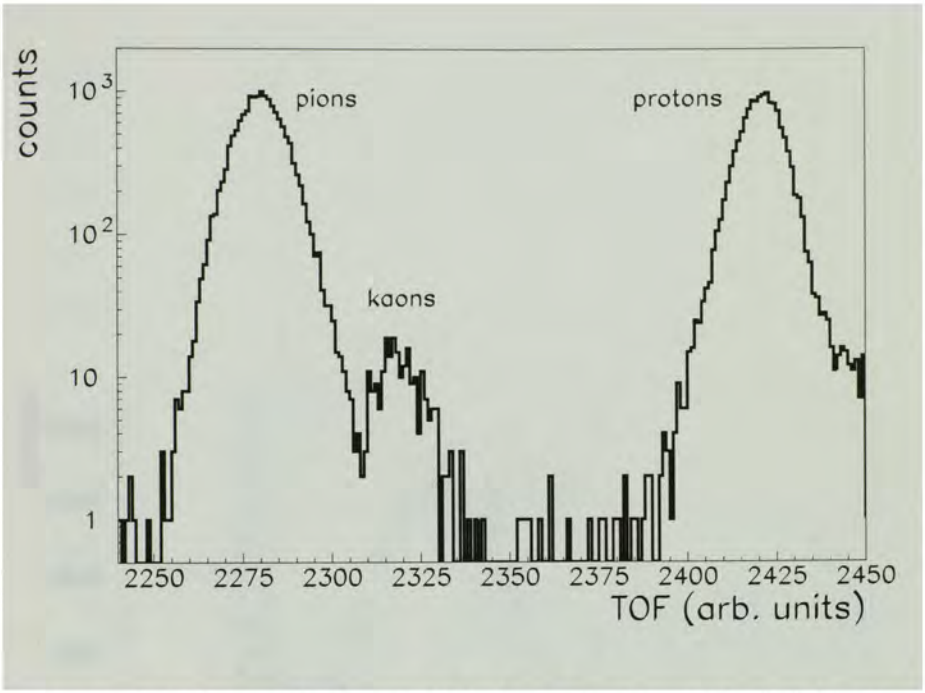

Figure 16: Time-of-flight distribution (TDC channel) after pulse-height corrections. Note the kaon peak is far more distinct than before.

beam line for cross reference. Shown in Fig. 17 and Fig. 18, respectively, are the typical responses of the first PMT (at +1800V with amplifier) and second PMT (at -2400V without amplifier), which are hereof referred to as "setting 1". As indicated in the figures, three distinct peaks can be seen in both cases. The pedestal is a measure of the offset within the electronics. When calibrating the distribution, this offset is simply subtracted out. The one photoelectron peak (1st pe) is the output of the PMT for only one photoelectron. From the separation between the pedestal and the first photoelectron peak, one can calibrate the axis into 'Number of Photoelectrons' by a linear formula:

$$N_{pe} = \frac{ADC_{raw} - pedestal}{1st_{pe} - pedestal} \tag{7}$$

Using Eq.7, along with PID cuts for pions, the uncalibrated distributions of the first and second tube transform into the calibrated plots shown in Fig. 19 and

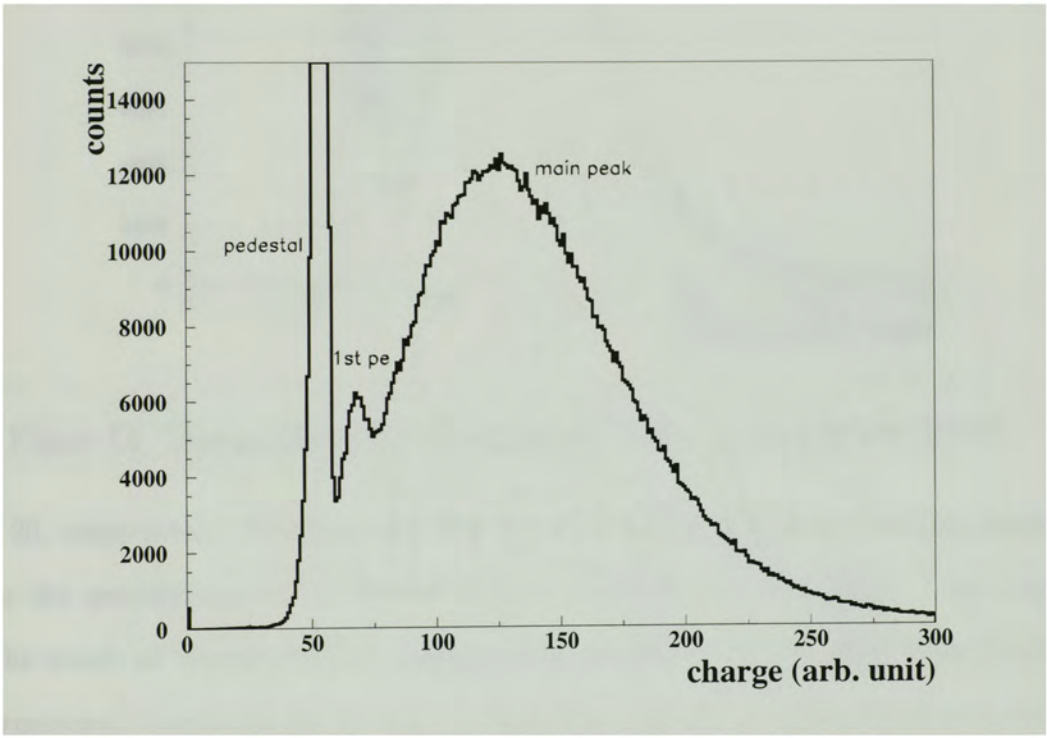

Figure 17: A typical uncalibrated output (ADC channel) of a PMT at +1800V (with amplifier) under experimental test conditions at 1.2 GeV/c. The pedestal corresponds to no light seen. The first photoelectron peak is used to calibrate the up to now uncalibrated axis into 'number of photoelectrons seen'. The main peak is the light detected for particles passing through the aerogel.

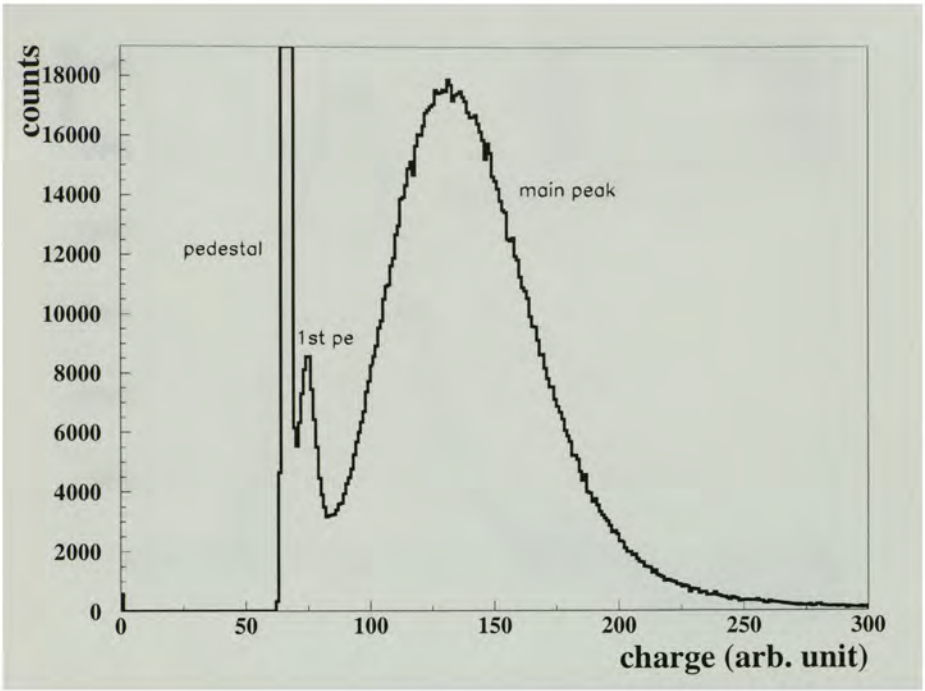

Figure 18: The uncalibrated ADC spectrum of the second tube at -2400V.

Fig. 20, respectively. Note here that the first tube performed worse than the second, since the average number of photoelectrons is less in the first tube. This might be the result of transportation damage when the tubes were shipped from Florida International University all the way to Tsukuba, Japan. When both tubes operate at their expected performance (as with the cosmic ray test at FIU), the number of photoelectrons was higher.

The sum of both tubes for pions at 1.2 GeV/c is shown in Fig. 21. As shown, one was able to observe 15.20 photoelectrons.

Runs at a higher voltage ("setting 2") were taken in order to investigate the optimal performance of the detector under experimental conditions. Fig. 22 show the result for this higher voltage setting. This time, on average 20.5 photoelectrons were observed, which is in reasonable agreement with the 19.8 photoelectrons predicted

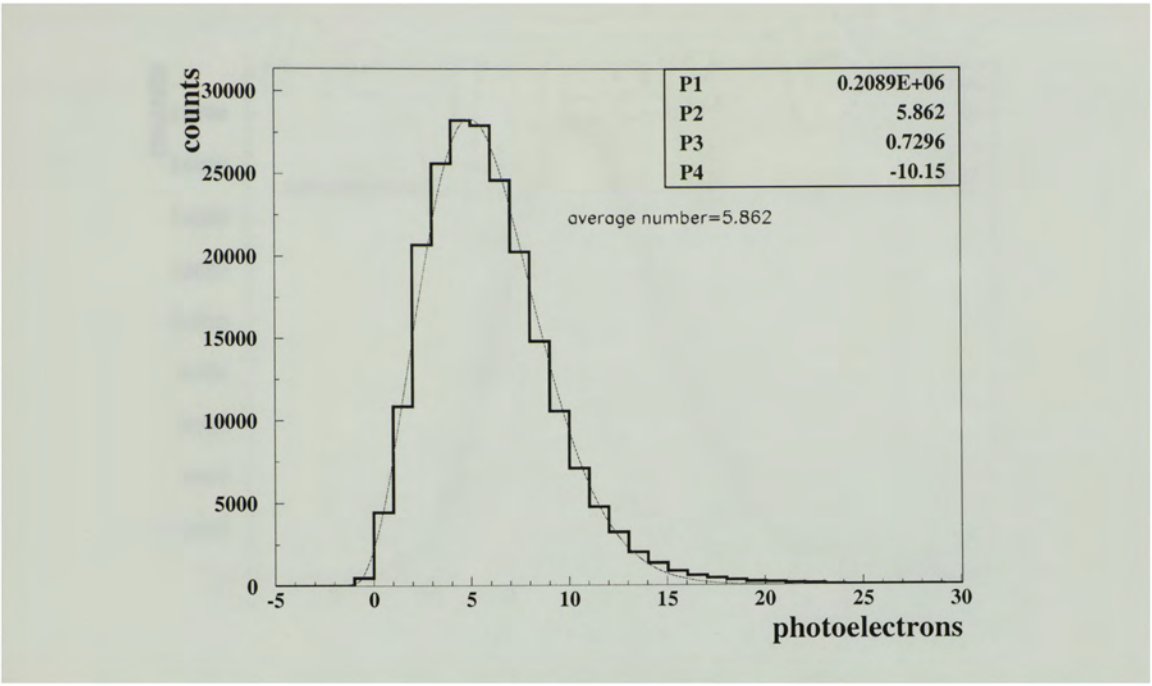

Figure 19: Yield in photoelectrons for pions at 1.2 GeV/c of the first tube along with the poisson fit of the distribution. Its performance was not as good as expected maybe due to damage to the tube or amplifier.

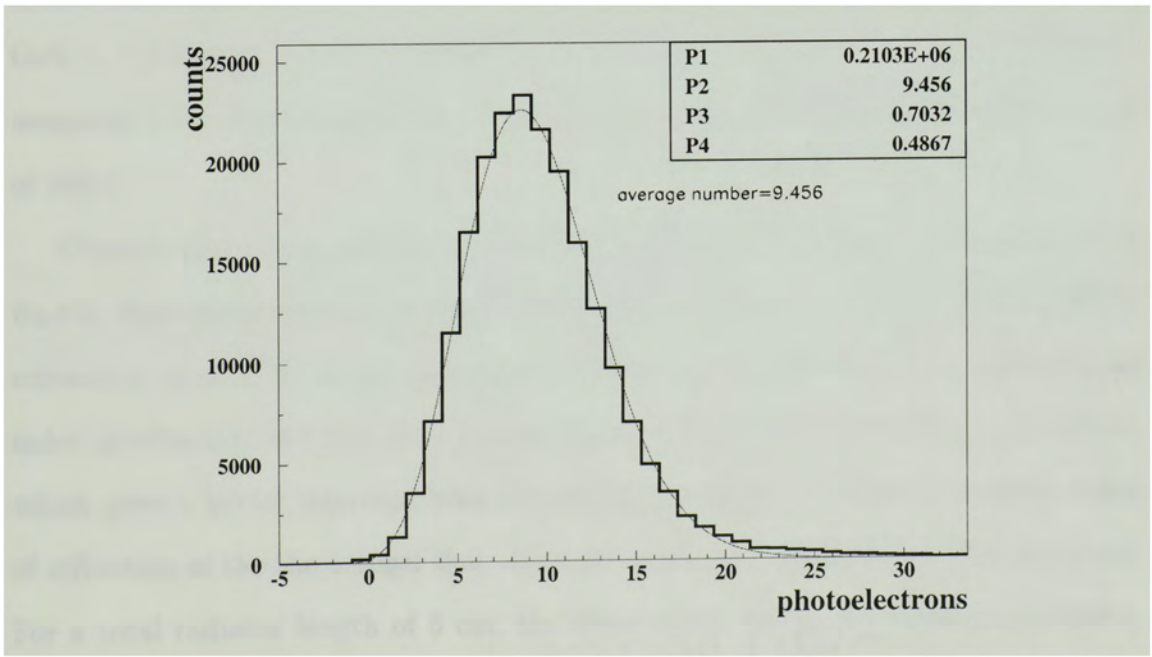

Figure 20: Yield in photoelectrons for pions at 1.2 GeV/c of the second tube along with the poisson fit of the distribution.

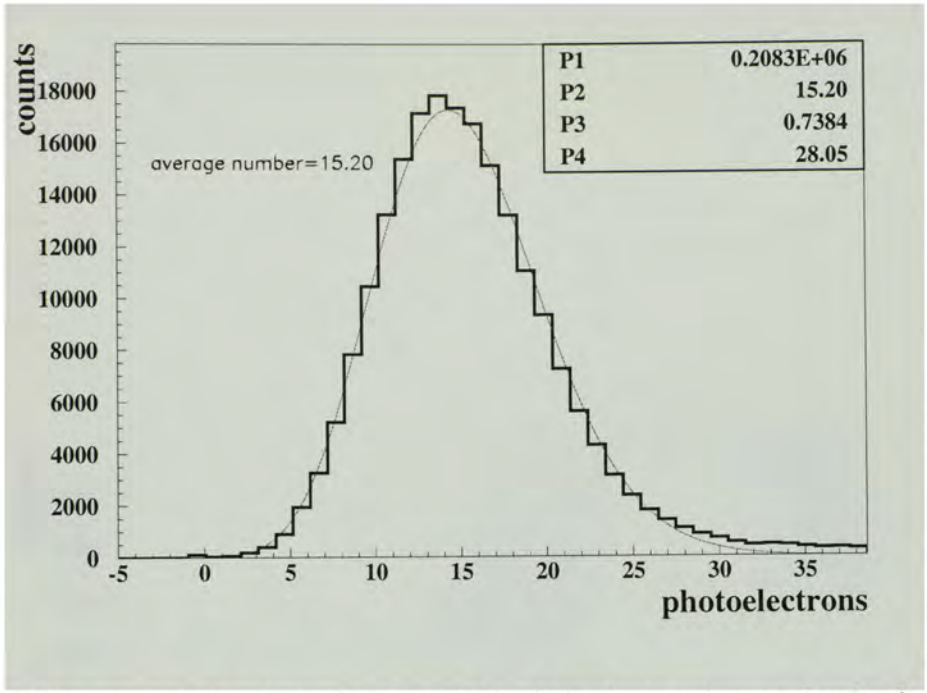

Figure 21: The sum of the photoelectron yield of the first and second tube for pions at 1.2 GeV/c along with the poisson fit of the distribution.

by the simulation of Section 4.1.2. The results for all momenta (0.5 GeV/c, 1.05 GeV/c, 1.2 GeV/c, 1.35 GeV/c) are shown in Fig. 23. θ_c was calculated from Eq.(2) assuming n = 1.055. Shown also is the fit of the data to $\sin^2\theta_c$, which yield a slope of 288.4.

Observe that the graph does not intercept the origin as suggested by Eq.(4) or Eq.(5). Speculation have been made of whether a deviation from the stated index of refraction, n, of 1.055 might be responsible for this. Just for reference, assuming an index of refraction of 1.045, the equation of the fit becomes: $(283\pm1)*x+0.12\pm0.07$, which gives a better intercept with the origin. Attempts to verify the correct index of refraction of the the aerogel that was used have unfortunately not been made yet. For a total radiator length of 5 cm, the slope of the linear fit of the data is 288.4. Therefore, the normalized slope (to 1 cm radiator length) is 57.7 cm^{-1}. Using Eq.(5) this could be interpreted as a collection efficiency of only about 58%. This can be

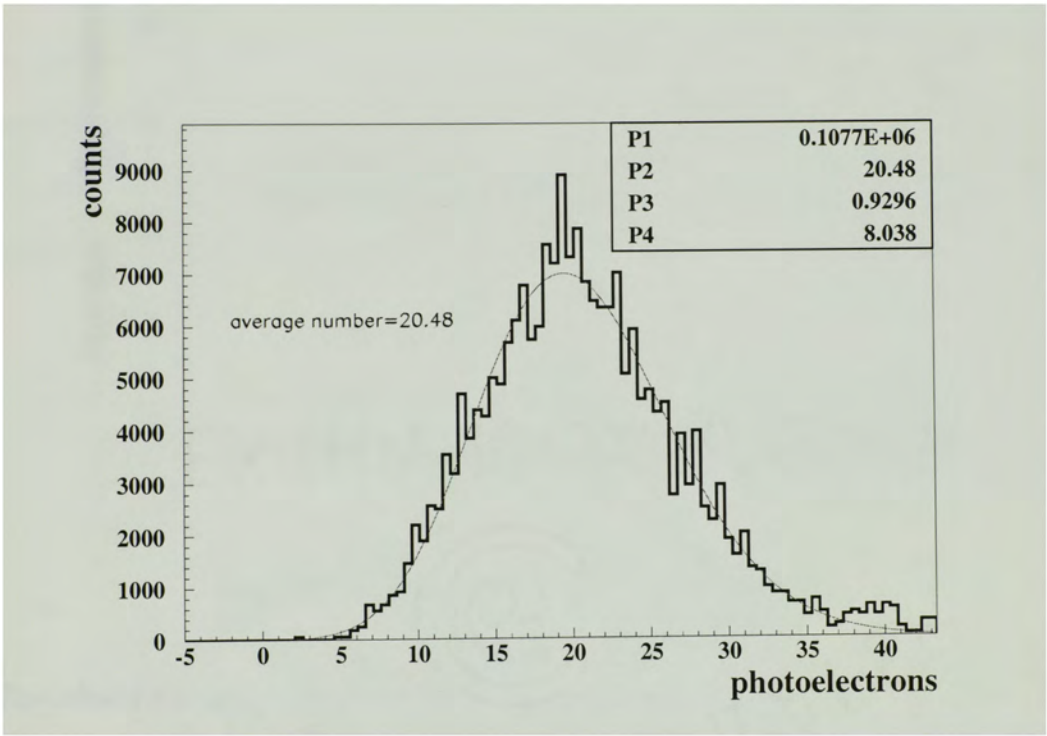

Figure 22: The sum of the photoelectron yield along with the poisson fit of the distribution of the first and second tube for pions at 1.2 GeV/c at +2000V and -2200V, respectively.

partially attributed to the loss of collection efficiency due to the partitioning (recall the factor of 1.2 mentioned in Section 4.1.1 which would scale our result to roughly 70 cm^{-1}).

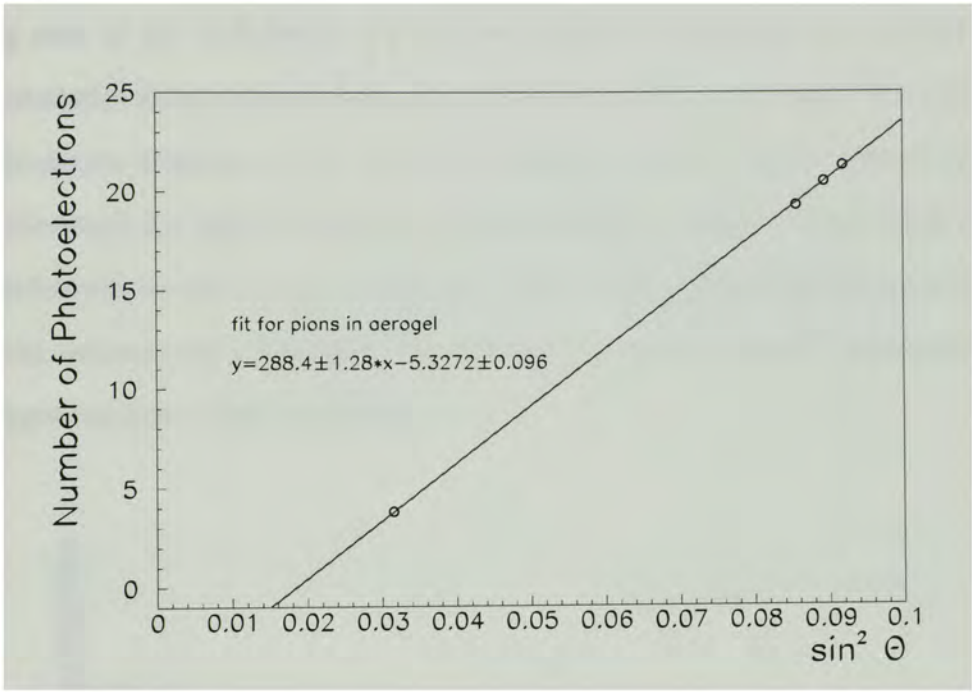

Figure 23: Photoelectron yield versus $\sin^2\theta_c$.

The numerical results for the four different momenta are summarized in Table. 2.

Momentum	Aerogel Yield
0.5 GeV	3.8 ± 0.1
1.05 GeV	19.3 ± 0.1
1.2 GeV	20.5 ± 0.1
1.35 GeV	21.3 ± 0.1

Table 2: Measured yield in photoelectrons for pions at different momenta.

In the hypernuclear experiment it is planned to set the trigger threshold on individual tubes. Therefore, with more photoelectrons detected per tube, one can set the trigger threshold higher without additional pions leaking into the data acquisition.

At the same time the kaon loss reduces. In order to investigate the detection efficiency of the full setup at "setting 2", the probability for a pion to produce a signal below a certain threshold number of photoelectrons was calculated by dividing the running sum of the distribution for the minimum of both tubes by its total sum. The probability for accidental kaon veto was calculated the same way. The results of this calculation is shown in Fig. 24 for pions and Fig. 25 for kaons. Since kaons are below threshold for light production, the probability to detect a kaon (that means not accidentally to veto on it) is basically 1 above only a few photoelectrons trigger threshold, whereas the probability for a pion not to veto is rapidly increasing with the trigger number of photoelectrons.

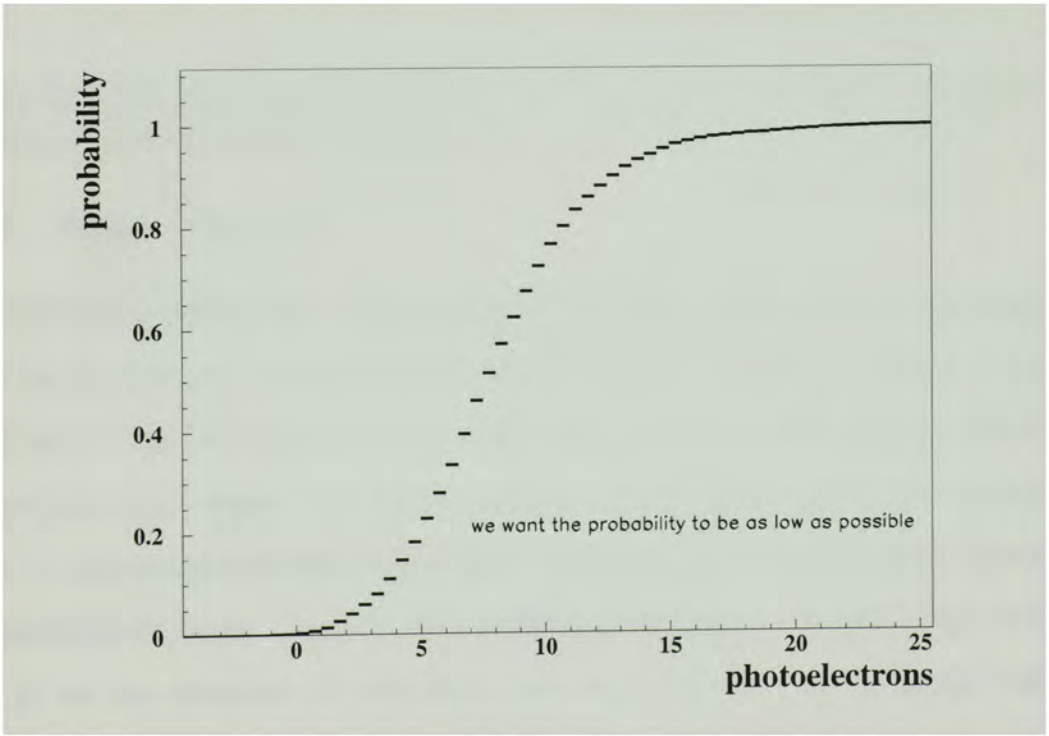

Figure 24: The probability of a pion not to set a veto versus the threshold number of photoelectrons for "setting 2".

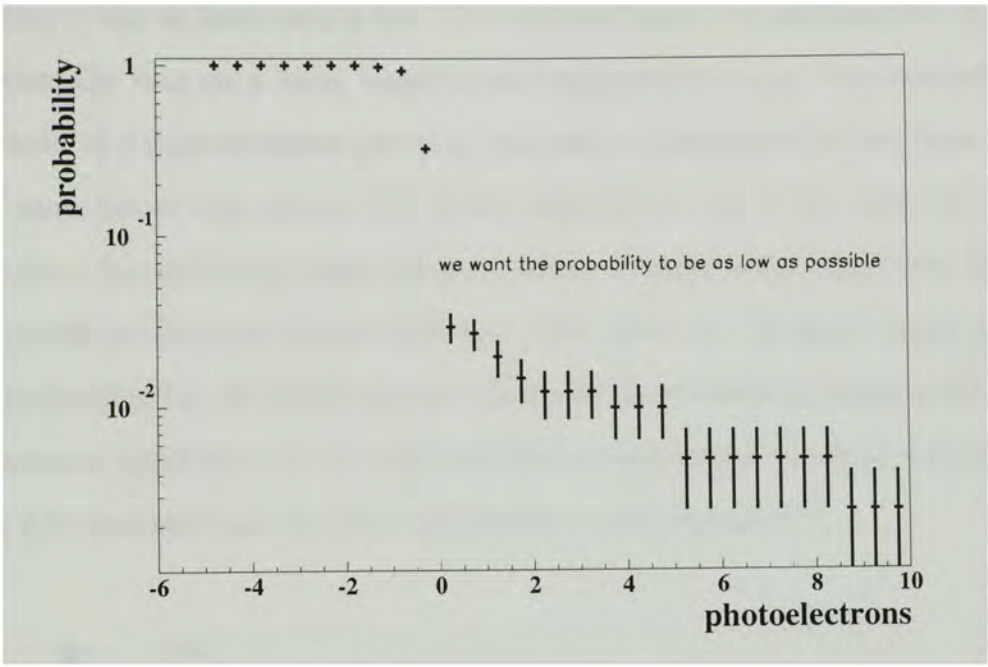

Figure 25: The probability of an accidental veto on a kaon versus the threshold number of photoelectrons for "setting 2".

4.1.5 Trigger efficiencies

The final full assembly of the aerogel Čerenkov detector used in Hall C will contain three layers of the partitioned detector. The layers will be arranged as shown in Fig 7 (right side). The particles have to cross all three layers, therefore allowing different trigger logic (e.g. require only one or two out of three layers to fire for a pion) in order to optimize simultaneous suppression of the high pion rate and positive particle identification for kaons. Using the probabilities for one layer as shown in Fig. 24 and Fig. 25 for the minimum of both tubes, one can extrapolate the resulting trigger efficiency of the full assembly. The results for the trigger efficiencies for 'one out of three' logic is shown in Fig. 26. The results for the trigger efficiencies for 'two out of three' logic is shown in Fig. 27. If one requires only one out of three layers to generate a veto, the probability that a pion traverses through all three layers without

generating a veto at least once is low. On the other hand, one increases the chance to accidentally veto on a kaon, which is not supposed to do so. For example, at a threshold of 2 photoelectrons per tube, the pion contamination is less than 10^{-4} with a kaon loss of only around 5%. If one requires two out of the three layers as a pion veto, the accidental kaon loss goes down, however more pions than before pass through the detector without detection. The 'three out the three trigger' logic, which is shown in Fig. 28, yields the best results for kaon detection, however the pion suppression is insufficient for the requirements on the detector. Even at a threshold of only 0.5 photoelectrons the pion surpression is only around 10^{-2}.

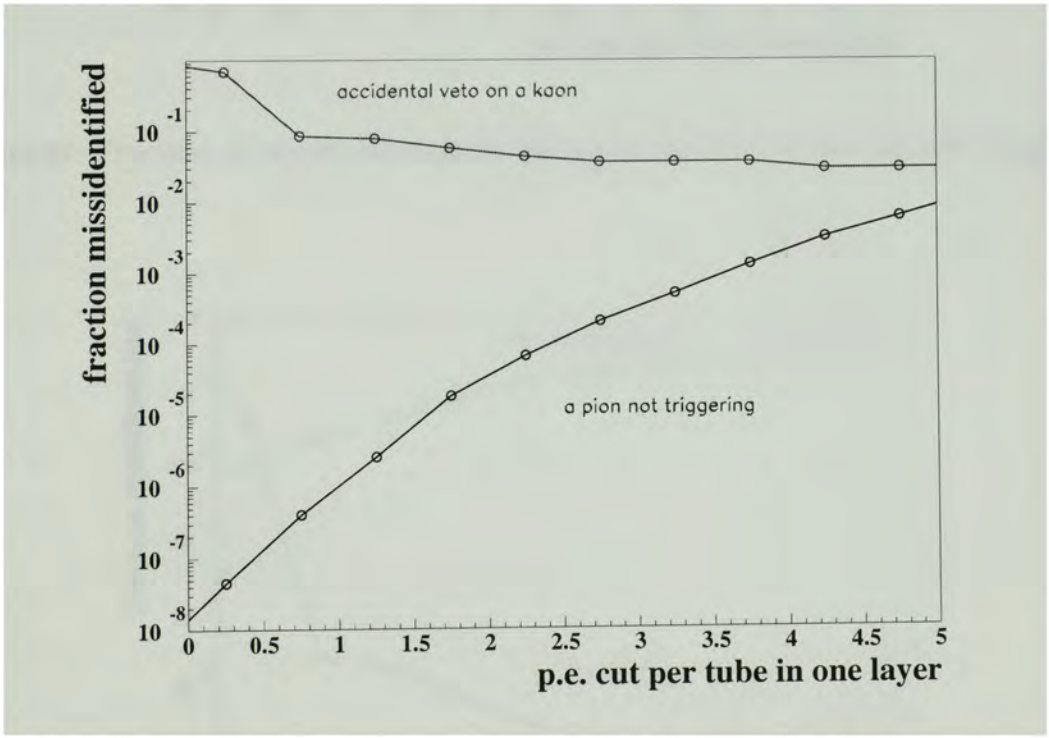

Figure 26: Fraction of misidentified pions and kaons for the 'one out of three' trigger logic. A misidentified pion is a pion not vetoing. A misidentified kaon is a kaon that does set the veto.

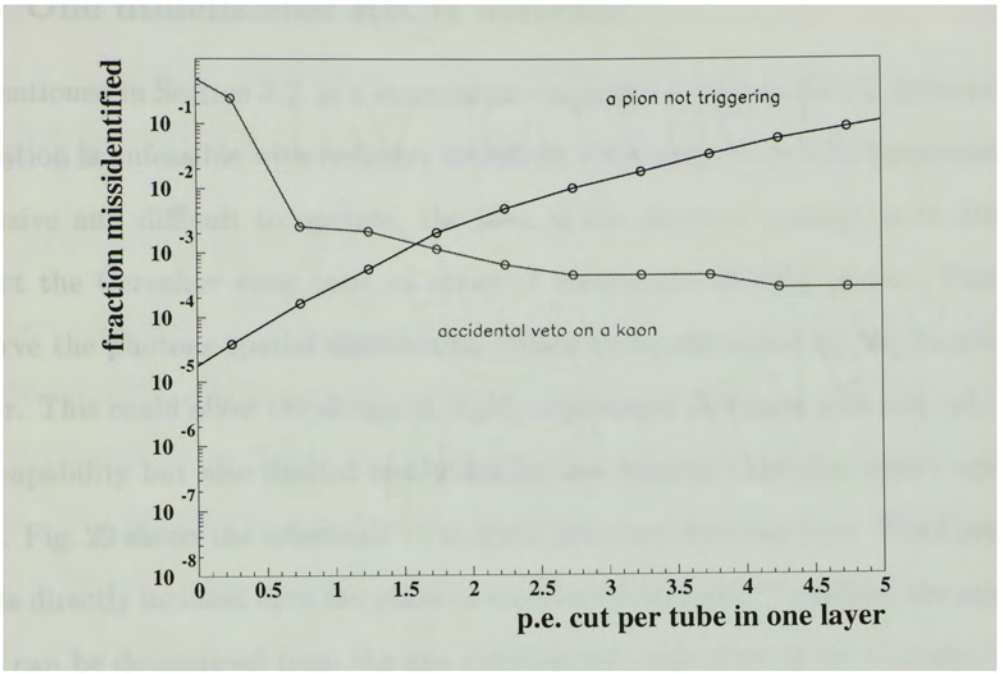

Figure 27: Fraction of misidentified pions and kaons for the 'two out of three' trigger logic.

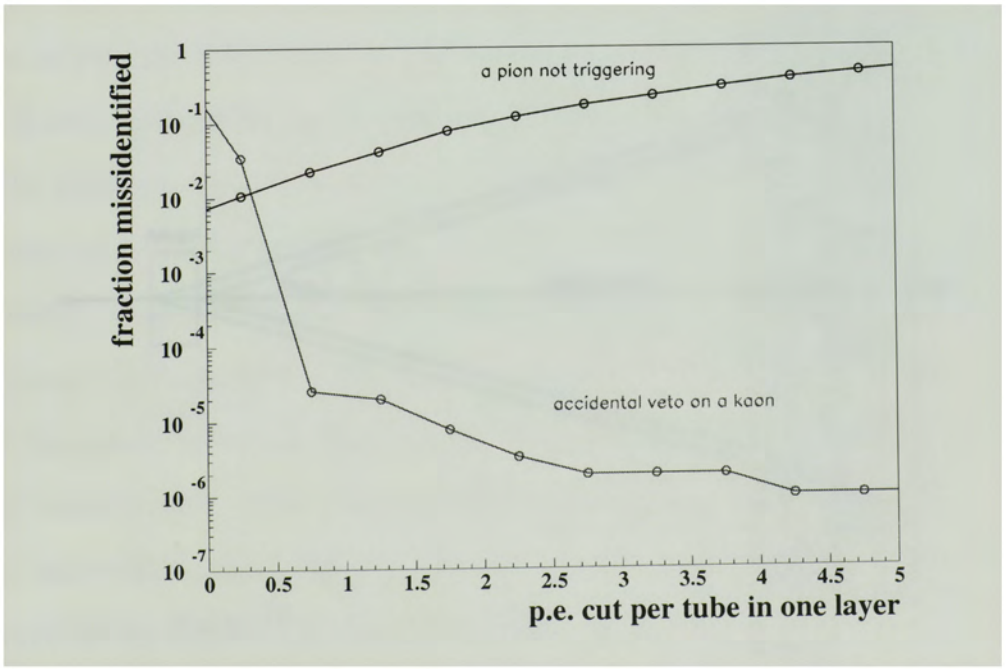

Figure 28: Fraction of misidentified pions and kaons for the 'three out of three' trigger logic.

4.2 One dimensional RICH detector

As mentioned in Section 3.2, in a momentum range of 5.5 GeV to 9 GeV, kaon-proton separation is unfeasible with ordinary threshold detectors. Since RICH detectors are expensive and difficult to operate, the idea of the detector concept is to directly project the Čerenkov cone onto an array of wavelength shifting plates. This will preserve the photons spatial distribution before being converted by the wavelength shifter. This could allow the design of highly segmented detectors with not only high rate capability but also limited resolution for the original Čerenkov cone's opening angle. Fig. 29 shows the schematic view of the proposed detector type. The Čerenkov cone is directly incident onto the plane of wavelength shifters. Therefore, the opening angle can be determined from the one dimensional projection of the Čerenkov ring. The light collection of the Čerenkov radiation is discussed in the following sections.

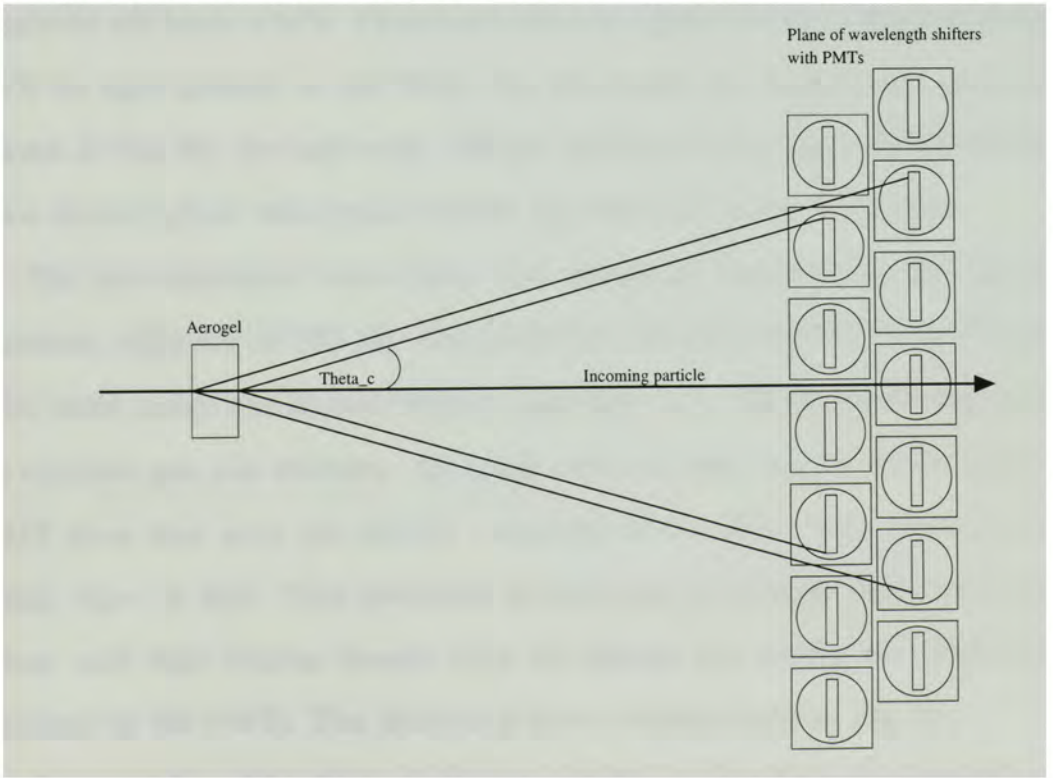

Figure 29: Schematic view of the wavelength shifter RICH detector concept.

The test counter is described in Section 4.2.1. The experimental setup and procedure is outlined in Section 4.2.2. The analysis and results are presented in Section 4.2.3, followed by a discussion and outlook in Section 4.2.4.

4.2.1 Detector description

In order to demonstrate the general feasibility, a simple test setup has been built to test the collection efficiency of the wavelength shifter bar. This system consisted of a 5-cm-thick stack of aerogel tiles placed 6 cm in front of an acrylic wavelength-shifting plastic. The aerogel tiles had an index of refraction of 1.055 and dimensions of 115 $\times$ 115 $\times$ 10 mm^3 (Matsushita SP-50 [3]). As wavelength shifter a 1.3 cm $\times$ 10.2 cm $\times$ 30.5 cm acrylic plate with an index of refraction of 1.49 was used. The acrylic plastic contained a wavelength shifting fluorescent additive [20] with a waveshifting quantum efficiency of 84%. This would result in a light collection efficiency of roughly 41% for light incident on the WLS. The absorption and fluorescence spectrum are shown in Fig. 30. On both ends, 130 mm photomultiplier tubes (XP4572B/D1 [4]) were directly glued with optical cement (BC-600 [21]) to the WLS plate.

The photomultiplier tubes have their maximum sensitivity at 420 nm with a quantum efficiency of 24% [4], thus, perfectly matching the WLS's peak emission. The entire setup was housed inside a light-tight box. Black plastic film was used as entrance and exit windows. All inside surfaces, including the active areas of the PMT faces that were not directly connected to the WLS, were covered by black paint, tape, or film. This prevented re-scattering of photons from these surfaces. Thus, only light coming directly from the aerogel and hitting the WLS could be detected by the PMTs. The detector is shown schematically in Fig. 31.

For particles with $v/c = 1$, Čerenkov light emitted from the aerogel reaches a maximum opening angle of 18.6 degree. On the 10.2 cm wide WLS plate this

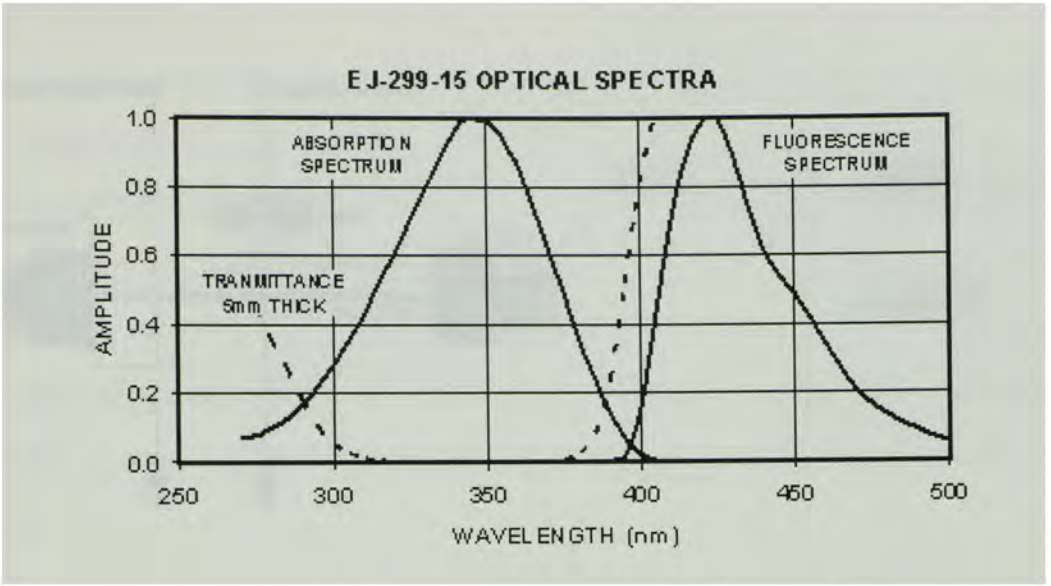

Figure 30: Absorption and fluorescence spectrum of the wavelength shifting plastic [20].

corresponds to ring radii ranging from 2 to 3.7 cm for the Čerenkov cones emitted from the 5 cm thick aerogel radiator. Čerenkov light from the aerogel incident on the plastic bar, as well as Čerenkov light directly produced within the bar, is converted into a frequency band of longer wavelength (425 nm) and isotropically re-emitted. The index of refraction of the acrylic plastic of $n = 1.49$ corresponds to a critical angle of 42 degree for total internal reflection. For the isotropically re-emitted light it follows that roughly 49% of the total solid angle is available for light transport toward the PMTs by total internal reflection.

4.2.2 Experimental setup and procedure

Beam tests have been conducted in December of 2002 at the KEK accelerator facility in Tsukuba, Japan. The detector was tested during the T530 beam test at the same beam line of the KEK 12 GeV proton synchrotron facility. The experimental conditions were almost identical as the ones described in Section 4.1.3. Again for reference, this beam line provides secondary beams with momenta up to 2 GeV/c

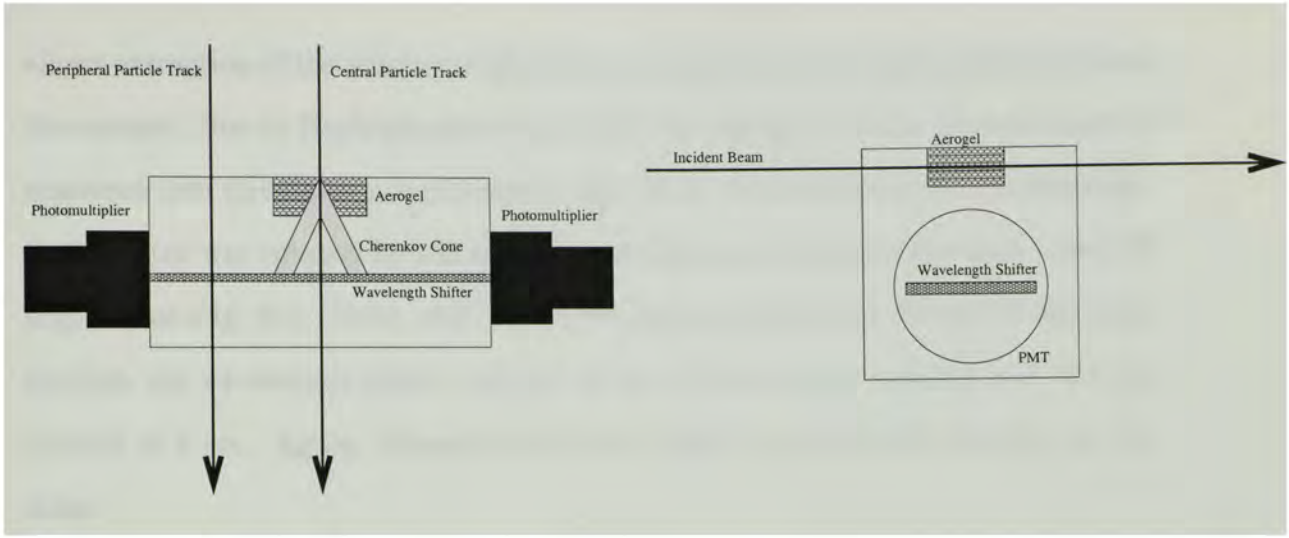

Figure 31: Schematic view of the detector. Left: Top view of normal (0 degree) orientation. For the 180 degree setting the particle tracks are in the opposite direction. Right: Side view of detector in 90 degree orientation.

and a momentum bite of roughly 1%. Secondary hadron beams of pions, kaons and protons were extracted at momenta of 0.50, 0.75, 1.05, 1.20, and 1.35 GeV/c. The detector described in Section 4.2.1 and several other prototype detectors were arranged behind a dipole magnet used for momentum selection. Two small scintillator crosses in the front and the back of the detectors served as time-of-flight detectors for particle identification. These time of flight (TOF) detectors actively collimated the beam to an envelope of 4×4 cm^2. Refer to Fig. 12 for the experimental setup, which was similar to the one used for the diffusion box aerogel Čerenkov detector. At all momenta, pions were above the WLS's as well as the aerogel's Čerenkov threshold. Kaons were below the aerogel threshold and above the WLS's thresholds at all momenta. Protons were above the WLS's thresholds at 1.05, 1.20, and 1.35 GeV/c and below the aerogel's threshold at all momenta. Data were taken with the beam passing through the center of the detector where the aerogel was located. As reference runs, the detector was moved to the sides, so that the particles only hit the WLS without passing through the aerogel. The difference of light output for pions

allows extraction of the number of photoelectrons produced by light originating from the aerogel. Due to Rayleigh scattering within the aerogel radiator photons may be scattered into directions not covered by the WLS. To investigate this qualitatively, the detector was rotated by 180 degree – particles entering from the back – and 90 degree (see Fig. 31). Note, that in the 90 degree setting, the beam did not pass through the wavelength shifter and the length of the aerogel radiator was 11.5 cm instead of 5 cm. Again, reference runs were taken by moving the detector to the sides.

4.2.3 Analysis and results

A typical pulse-height corrected time-of-flight (TOF) distribution, which is similar to Fig. 16 is shown in Fig. 32.

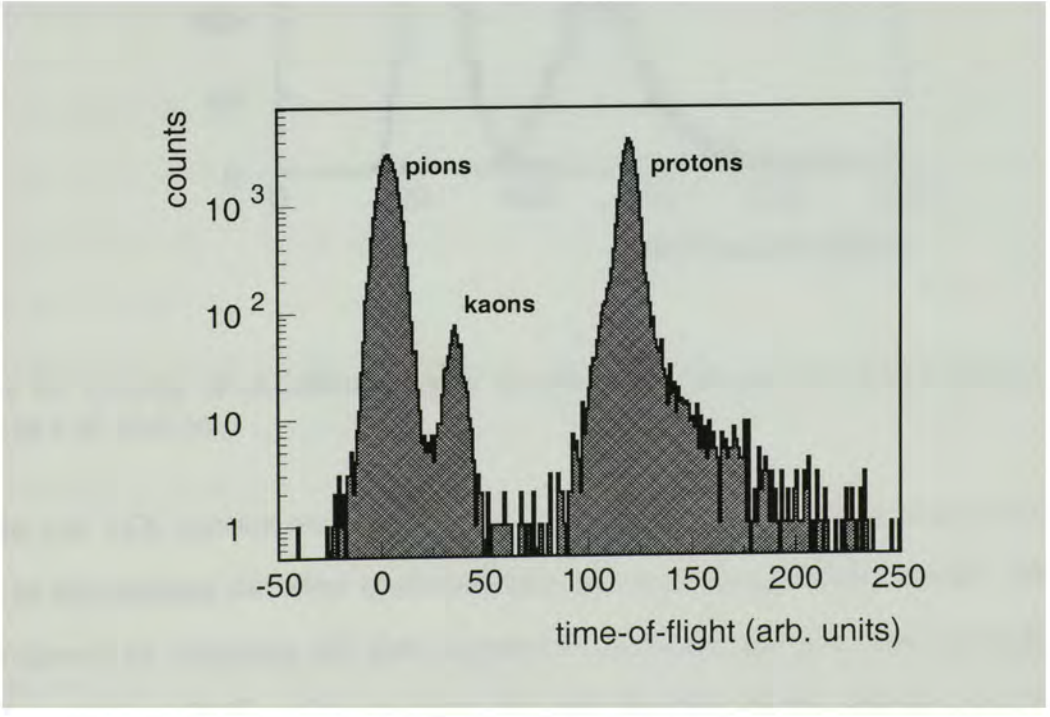

Figure 32: Time-of-flight distribution for the RICH detector setup.

Again, pions (left peak), kaons (small center peak) and protons (right peak) were unambiguously identified. As for the threshold aerogel Čerenkov detector, cuts were placed on these TOF distributions. In Fig. 33 a typical response of a single PMT is shown. Two separated distributions can be seen, corresponding to protons and pions, respectively. Only the pion distribution is expected to contain light from the aerogel radiator.

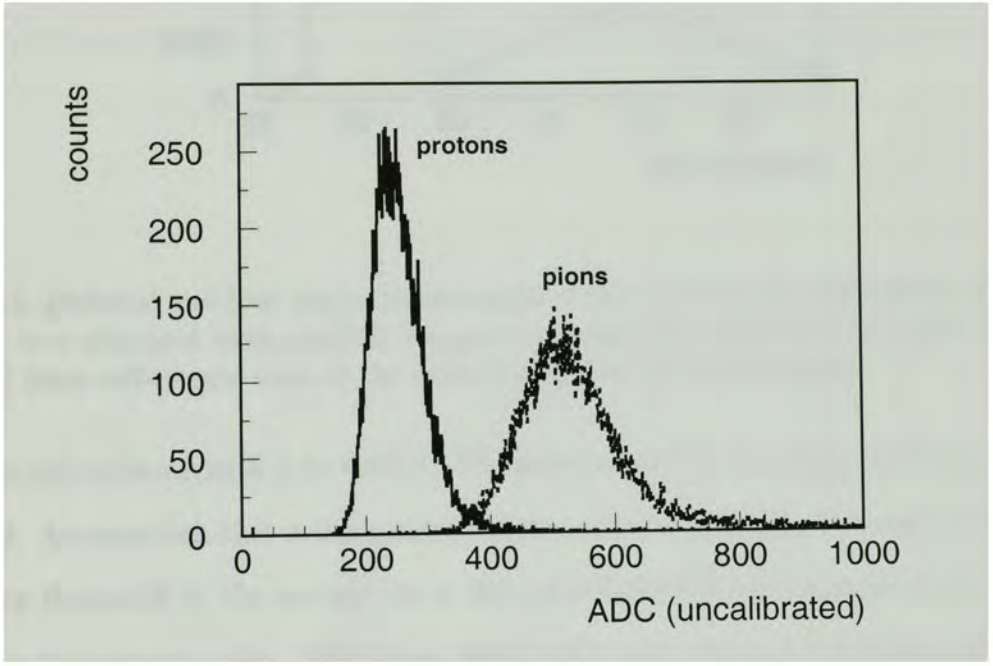

Figure 33: Overlay of uncalibrated ADC distributions for one tube for protons and pions at 1.35 GeV/c.

The raw ADC spectra were calibrated to the corresponding number of photoelectrons by determining the offset (pedestal) and one photoelectron distributions. This was achieved by triggering the data acquisition randomly and with low thresholds on the individual PMTs. Fig. 34 shows the superposition of the pedestal and the one photoelectron peak.

Fig. 35 shows the calibrated sum in photoelectrons of the left and right PMT

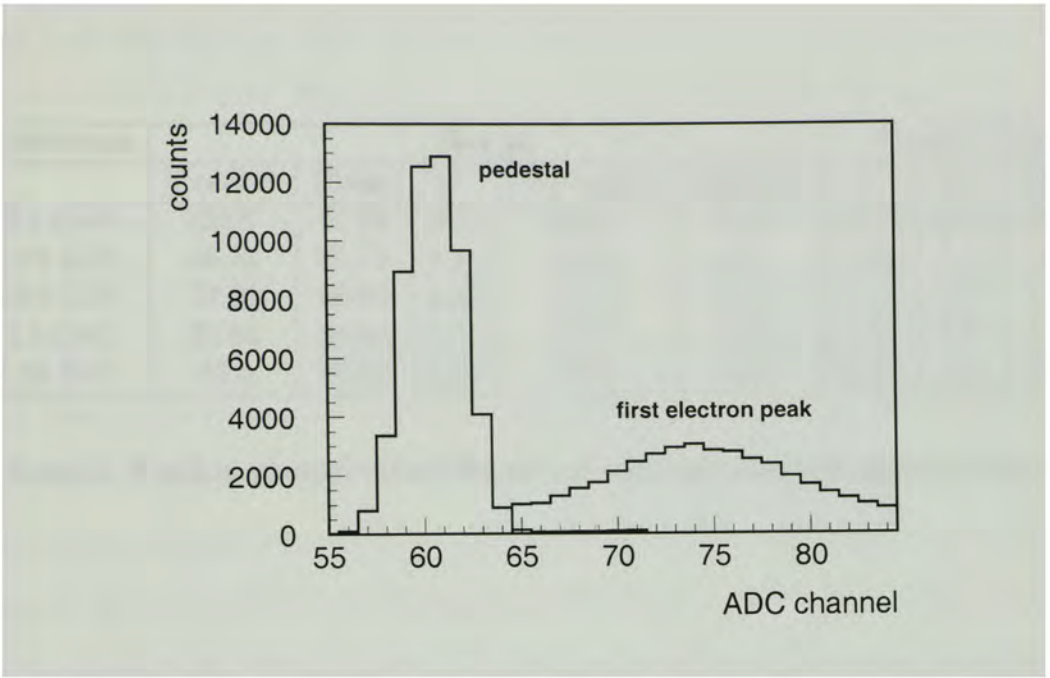

Figure 34: Pedestal and first photoelectron peak of one tube for the calibration. The pedestal was obtained from random trigger runs, the first photoelectron peak was obtained from self-trigger runs of the individual tubes at low threshold.

for pions and protons with 1.35 GeV/c. For protons, 19.9 ± 0.1 photoelectrons are observed. As expected, this is independent of the detector position, because protons are below threshold in the aerogel, so it does not matter if they pass through the center or through the side. For pions, 66.8 ± 0.1 and 73.0 ± 0.2 photoelectrons are observed for the peripheral and central settings, respectively. This indicates a contribution of 6.2 ± 0.3 photoelectrons from the aerogel radiator. The results for all momenta are summarized in Table 3.

4.2.4 Discussion

The photoelectron yield for particles below the aerogel threshold, protons and kaons at all momenta and pions in the peripheral settings, allows the extraction of the intrinsic response of the wavelength shifter. Fig. 36 shows this yield versus $\sin^2 \theta_c$.

Momentum	Setting					Aerogel Yield		
	0°*center*	0°*side*	90°	180°*center*	180°*side*	0°	90°	180°
0.5 GeV	62.67	62.98	0.26	60.65	60.90	-0.31	0.26	-0.25
0.75 GeV	68.79	65.71	2.11	63.52	64.7	3.08	2.11	-1.2
1.05 GeV	72.37	66.63	3.33	67.16	65.83	5.74	3.33	1.33
1.2 GeV	72.64	66.83	3.51	67.27	66.04	5.81	3.51	1.24
1.35 GeV	73.0	66.82	3.64	67.7	66.0	6.18	3.64	1.75

Table 3: Yield in photoelectrons for several momenta and settings for pions.

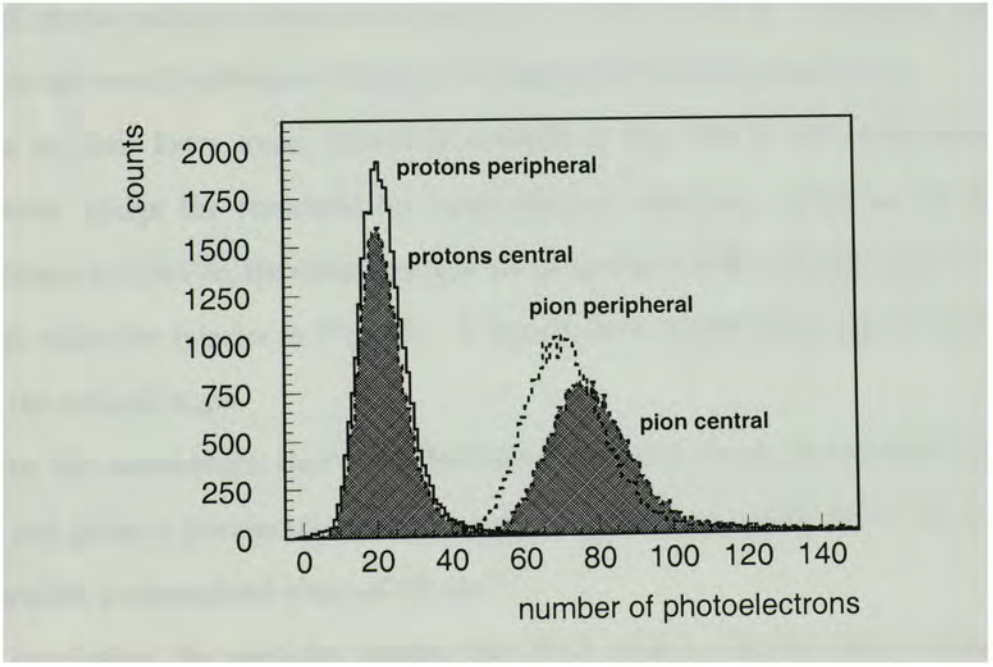

Figure 35: Combined light yield of both tubes for pions and protons at 1.35 GeV/c. The unshaded areas correspond to the peripheral reference runs. The shaded areas correspond to the central settings for which the aerogel light also contributes.

Here θ_c is the opening angle of the Čerenkov cone that would be expected for a radiator with $n = 1.49$. The yield for protons is shown with the triangles. The data point at $\sin^2\theta_c = 0$ corresponds to protons at 0.75 GeV/c momentum, below the WLS threshold (for the 0.5 GeV/c setting, protons were too slow to be recorded by the data acquisition gate). The line through the data shows a parameterization with the form $N_{\text{p.e.}} = N(0) + N_0 \times \sin^2\theta_c$. The two parameters $N(0)$ and N_0 have been obtained by a χ^2 minimization using the program package MINUIT [22]. The observed offset of $N(0) = 3.16 \pm 0.05$ could be due to, for example, a small scintillation component or high momentum δ-electrons. Normalizing the observed slope of $N_0 = 49.8 \pm 0.2$ to the radiator thickness of 1.27 cm gives 39.2 cm^{-1}. This can be compared to a "standard" detector with 90% collection efficiency and a typical bi-alkali photo-cathode which would yield $N/L = 90\text{cm}^{-1}\sin^2\theta_c$. Therefore, one can conclude an overall collection efficiency of roughly 39% for the test setup.

Due to their lower mass, kaons (X symbols in Fig. 36) at the same momenta as protons bridge the threshold for total internal reflection. Even at the lowest momentum, 0.5 GeV/c, the opening angle for pions is above the critical angle for total internal reflection (circles in Fig. 36). A significantly higher slope can be observed above the critical angle.

With the assumption that the offset observed for protons should also hold for kaons and pions a parametrization through the pion data yields $N_0 = 117.1 \pm 0.1$ This implies a normalized slope of 92 cm^{-1}.

In conclusion, for particles passing the WLS with a velocity that corresponds to an opening angle of the Čerenkov cone below the critical angle for total internal reflection, light outside the absorption band of the WLS (see Fig. 30) will penetrate the acrylic plate and is not available for detection. Therefore, the estimated 40% collection efficiency from the proton data can be used as a benchmark for the detection

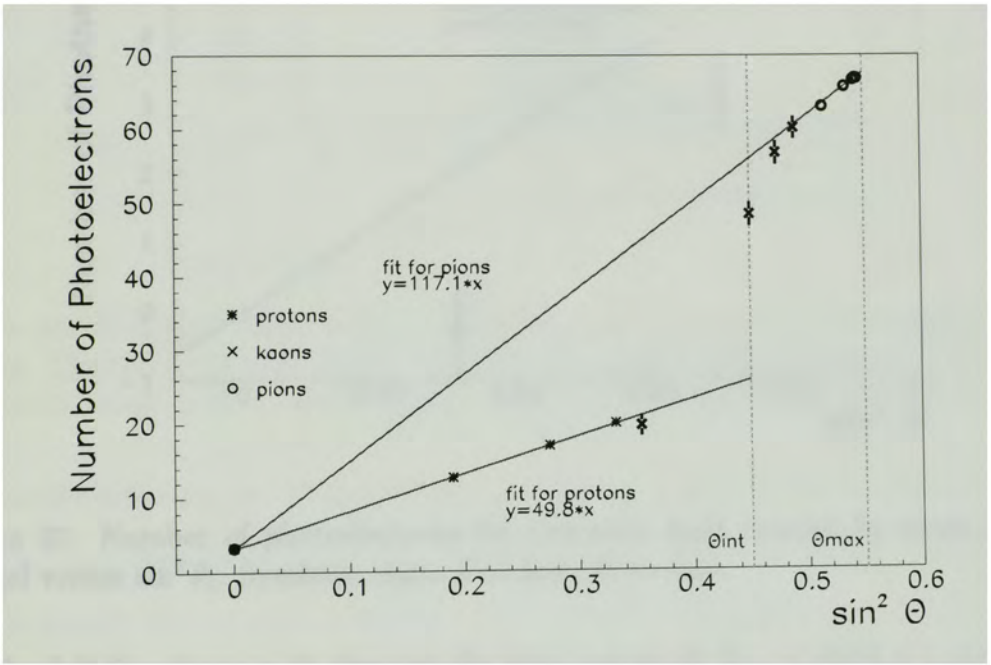

Figure 36: Number of photoelectrons for Čerenkov light created in the WLS versus $\sin^2\theta_c$. The vertical lines indicate the threshold for total internal reflection and the maximum Čerenkov angle. The diagonal lines show fits to the proton data (crosses) and the pion data (circles), respectively. Kaons data are represented by X symbols.

of light from the aerogel radiator.

Fig. 37 shows the extracted yield from the aerogel radiator. Note that the horizontal axis, $\sin^2\theta_c$, differs from Fig. 36 because of the lower index of refraction.

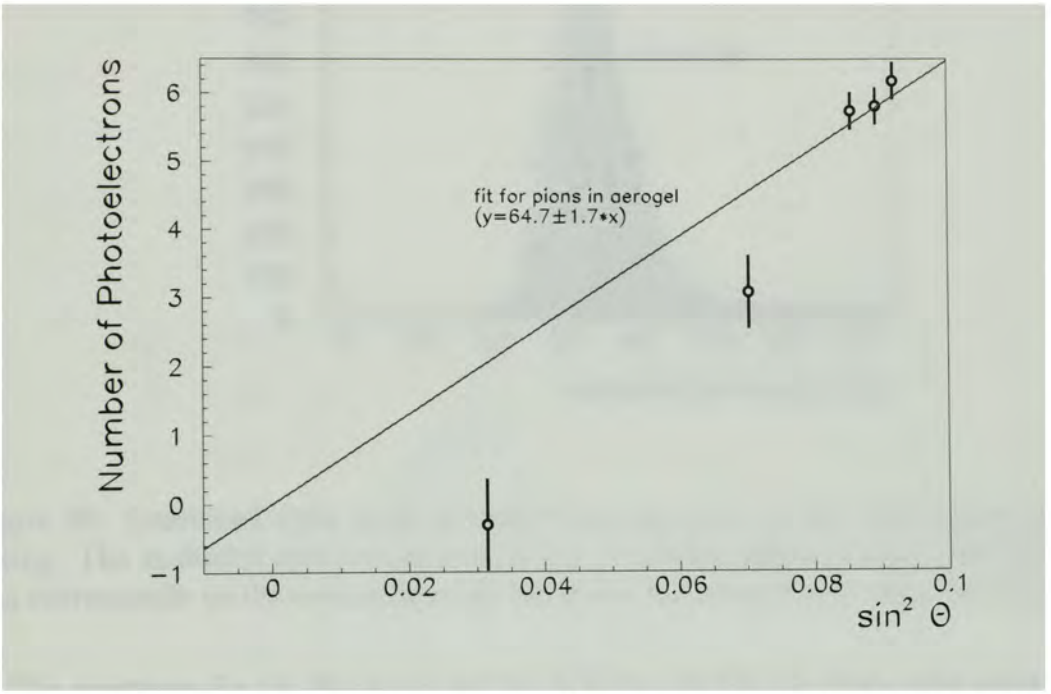

Figure 37: Number of photoelectrons for Čerenkov light created by pions in the aerogel versus $\sin^2\theta_c$. Symbols: data. Full line: fit to data.

The full line shows a fit through the data points of $N_{p.e} = (64.6 \pm 1.1)\sin^2\theta_c$. Normalized to the thickness of 5 cm, this yields 12.9 cm^{-1}, or a collection efficiency of roughly 13%. This is significantly lower than expected from the WLS's intrinsic response to protons. It can be understood, however, with the assumption that a significant fraction of the primary Čerenkov light is subject to scattering in the aerogel. Scattered photons then may not hit the WLS. This has been investigated qualitatively by rotating the entire detector as described in Section 4.2.2. When rotated by 180 degree – particles pass first the WLS and then the aerogel – 1.745 $\pm$ 0.34 photoelectrons are observed from the aerogel for pions at 1.35 GeV/c (see Fig. 38).

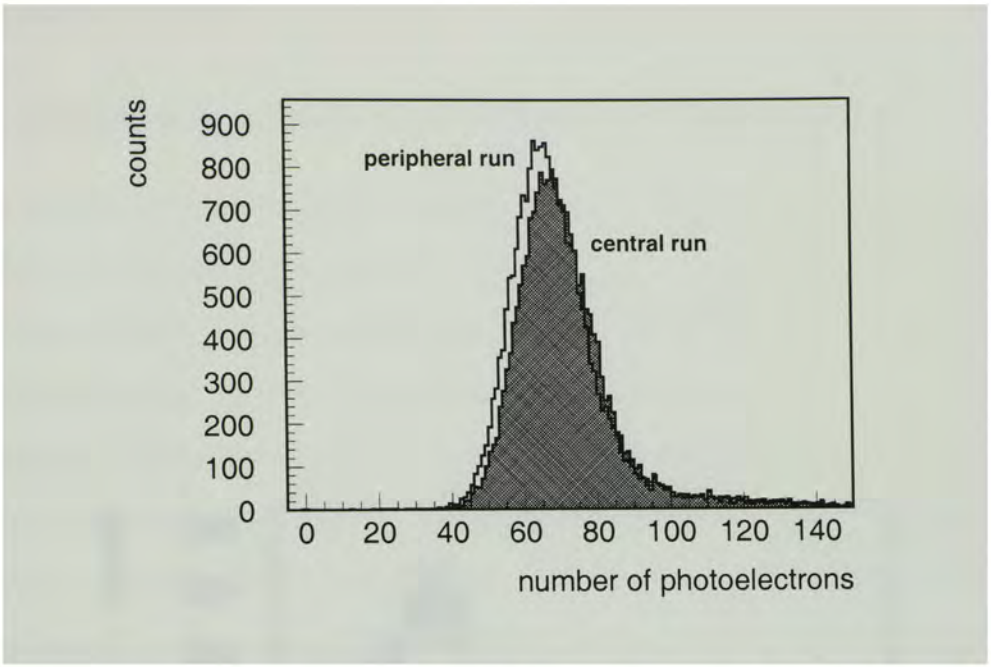

Figure 38: Combined light yield of both tubes for pions at the 180 degree angle setting. The unshaded area corresponds to the peripheral reference runs. The shaded area corresponds to the central settings for which the aerogel light also contributes.

The spectrum for the 90 degree setting is shown in Fig. 39. Note, that since the particle track does not intercept the wavelength shifter in this setting the observed yield is entirely due to pions radiating in the aerogel. Also the radiator length is now 11 cm instead of 5 cm. On average 3 to 4 photoelectrons are observed in this setting. As the WLS only covers only about 17% of the full azimuthal angle with respect to the particle track this result supports the hypothesis that the low collection efficiency for the normal setting is due to internal scattering inside the aerogel radiator.

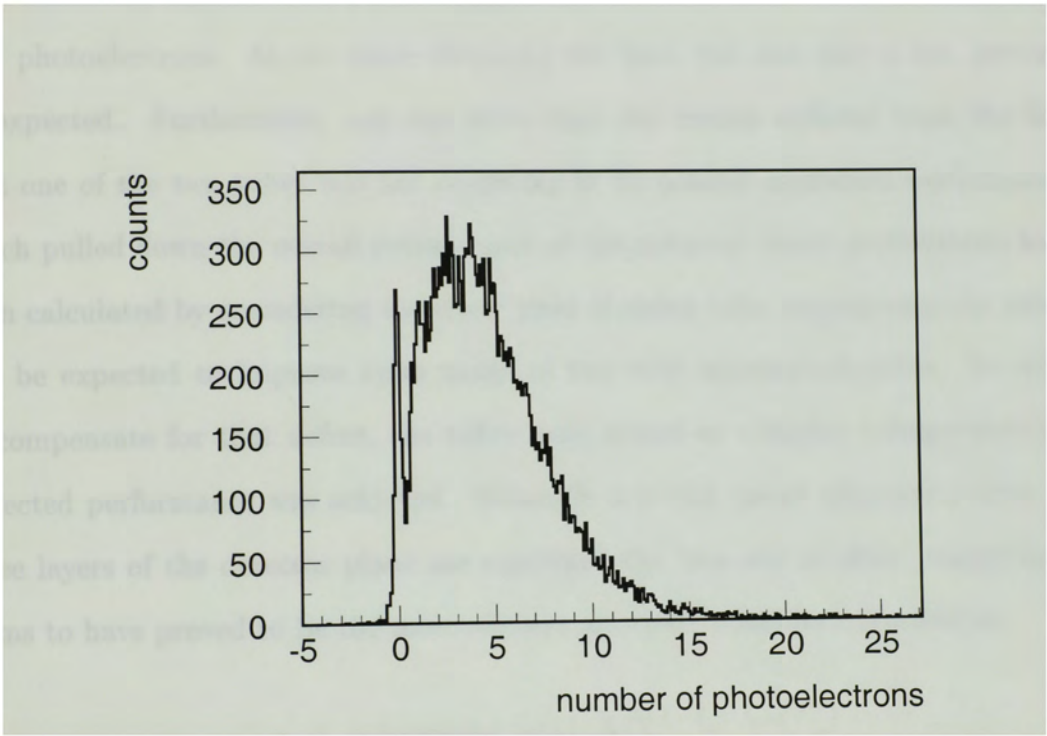

Figure 39: Combined light yield of both tubes for pions at the 90 degree angle setting. Note the fine resolution for single photoelectrons.

5 Conclusion

5.1 Partitioned threshold aerogel Čerenkov detector

As the analysis has shown, the partitioned aerogel Čerenkov detector has met, if not exceeded, the expectation put upon it. On average, more than 20 photoelectrons have been observed, which led to a pion suppression of better than 10^{-4} for a threshold of 2 photoelectrons. At the same threshold the kaon loss was only a few percent, as expected. Furthermore, one can state that the results suffered from the fact that one of the two tubes was not operating at its normal maximum performance, which pulled down the overall performance of the detector. Since probabilities have been calculated by considering the lower yield of either tube respectively, the result can be expected to improve upon usage of two fully operational tubes. In order to compensate for that defect, the tubes were tested at a higher voltage were the expected performance was achieved. Although it is still under discussion, when all three layers of the detector plane are combined the 'one out of three' trigger logic seems to have proved to be the most efficient alternative for the full assembly.

5.2 One dimensional RICH detector

The collection efficiency of a wavelength shifting acrylic plastic bar has been determined for Čerenkov light created within the plastic as well as Čerenkov light incident from an external aerogel radiator. For particle velocities that correspond to Čerenkov angles above the critical angle for total internal reflection, a collection efficiency of 92% has been observed. For emission angles below the critical angle, the collection efficiency is roughly 39%, close to the expected value of 41% as mentioned in Section 4.2.4. The collection efficiency for light from an external aerogel radiator could not be determined quantitatively because of scattering inside the aerogel. The re-

sults look promising enough, however, to warrant further investigation. Therefore, currently funds are being requested in order to build a more sophisticated prototype involving several wavelength shifters connected to smaller PMTs.

REFERENCES

1. See for example: J.D Jackson, *Classical Electrodynamics*, 3rd edition, (John Wiley & Sons, New York, 1998)

2. K. Hagiwara et al. [Particle Data Group Collaboration], Phys. Rev. D 66,010001 (2002).

3. Matsushita Electric Works, Ltd., 1408 Kadoma, Osaka 571-8686, Japan, (private communication).

4. Photonis Imaging Sensors, (private communication). Photonis Avenue Roger Roncier Z.I. Beauregard B.P. 520 19106 BRIVE Cedex.

5. Coman, Marius Master Thesis: *The Hall An Aerogel Cherenkov detector*, Florida International University, 2000 (unpublished).

6. R. M. Mohring, Dissertation: A comparison of longitudinal and transverse sections in the $p(e,e'K^+)\Lambda$ and $p(e,e'K)\Sigma^0$ reactions, 1999 (unpublished)

7. R. Perrino, "Performance of the aerogel threshold Cherenkov counter for the Jefferson Lab Hall A spectrometer in the 1-4 GeV/c momentum range," Nucl. Instrum. Meth. A 457 (2001) 571.

8. H. E. Jackson, "The HERMES dual-radiator RICH detector," Nucl. Instrum. Meth. A 502 (2003) 36.

9. R. De Leo, "Electronic detection of focused Cherenkov rings from aerogel," Nucl. Instrum. Meth. A 421 (1999) 249.

10. 3rd International Workshop on Ring Imaging Cherenkov Detector (RICH 98) 15-20 November 1998, Ein Gedi, Dead Sea, Israel. Proceedings: ADVANCES IN CHERENKOV LIGHT IMAGING TECHNIQUES AND APPLICATIONS: Proceeding. Edited by A. Breskin, R. Chechik, and T. Ypsilantis. Amsterdam, Netherlands, North- Holland, 1999. 578p. (Nuclear Instruments and Methods, Vol. A433, Nos. 1-2, August 1999, P. 1-578).

11. 4th Workshop on RICH Detectors: Dedicated to the memory of Tom Ypsilantis (RICH 2002) 5-10 June 2002, Pylos, and Greece. Home URL: http://www.nestor.org.gr/rich2002/

12. Spectroscopic study of Λ hyper nuclei up to medium-heavy mass region through the $(e,e'K^+)$ reaction, spokespersons: O. Hashimoto, S. N. Nakamura, J. Reinhold, and L. Tang.

13. T. Miyoshi, "High Resolution Spectroscopy of the ^{12}B Hyper nuclear produced by the (e,e'K^+) reaction, Phys. Lett. 90, 232502 (2003).

14. Hall C Conceptual Design Report; http://www.jlad.org/hallc/upgrade/cdr.pdf

15. D. W. Higinbotham, "Diffusely reflective aerogel Cherenkov detector simulation techniques," Nucl. Instrum. Meth. A 414 (1998) 332.

16. R. Suda, "Monte-Carlo simulation for an aerogel Cherenkov counter," Nucl. Instrum. Meth. A 406 (1998) 213.

17. 3M Scotch 665 Double-Coated Permanent Tape.

18. Millipore Corporation, Bedford, MA 01730

19. Bayer, M, Master Thesis, MIT, 1982 (unpublished).

20. ELJEN TECHNOLOGY, P.O. Box 870, 300 Cane Street, Sweetwater, TX 79556, U.S.A., (private communication).

21. Saint-Gobain Crystal & Detectors (Bicron) Les Miroirs – 18, Avenue d'Alsace – 92096 La Dfense 3 Cedex – France, BC-600: Optical Cement.

22. F. James and M. Roos, Comput. Phys. Commun. 10, 343 (1975).